

Maser Flares Driven by Variations in Pumping and Background Radiation

M. D. Gray^{1,2}, S. Etoka¹, A. Travis¹ and B. Pimpanuwat¹

¹*Jodrell Bank Centre for Astrophysics, Department of Physics and Astronomy, University of Manchester, M13 9PL, UK*

²*National Astronomical Research Institute of Thailand, 260 Moo 4, T. Donkaew, A. Maerim, Chiangmai 50180, Thailand.*

ABSTRACT

We simulate maser flares by varying either the pump rate or the background level of radiation in a 3D model of a maser cloud. We investigate the effect of different cloud shapes, saturation levels and viewpoints. Results are considered for clouds with both uniform and internally variable unsaturated inversion. Pumping and background variations are represented by several different driving functions, some of which are light curves drawn from observations. We summarise the pumping variability results in terms of three observable parameters, the maximum flux density achieved, a variability index and duty cycle. We demonstrate typical ranges of the flux density that may result from viewing an aspherical object from random viewpoints. The best object for a flare is a prolate cloud, viewed close to its long axis and driven from unsaturated conditions to at least modest saturation. Results for variation of the background level are qualitatively different from the variable pumping results in that they tend to produce short intervals of low flux density under conditions of moderate saturation and sufficient variability to be consistent with strong flaring. Variable background models typically have a significantly higher duty cycle than those with variable pumping.

Key words: masers – radiative transfer – radio lines: general – radiation mechanisms: general – techniques: high angular resolution – ISM: lines and bands.

1 INTRODUCTION

This paper is the third in a series that investigates several plausible mechanisms for maser flares. In Gray et al. (2018) (Paper 1), we investigated variability produced by the rotation of a quasi-spherical maser cloud. That work was extended to the rotation of approximately spheroidal oblate and prolate clouds in Gray et al. (2019) (Paper 2). The present work introduces the mechanisms of time-dependent variation in the pumping scheme and time-dependent variation in the background radiation amplified by the maser cloud. We do not rule out cloud overlap in the line of sight as a flare mechanism, but defer analysis of the overlap mechanism to a later paper in this series.

We define a variability index for the purposes of this work as F_{pk}/F_{qui} , where F_{pk} is the line centre flux density at the flare maximum and F_{qui} is the corresponding flux density under quiescent conditions. If the light curve has no flat quiescent state, F_{qui} defaults to the minimum flux density. The oblate and prolate clouds studied in Paper 2 can produce flares with variability indices of thousands in optimal viewing planes, but more typically of order tens for a randomly placed observer. Rotation of the pseudo-spherical object in Paper 1 produces variability index values of ~ 3 . Stability considerations strongly suggest that rotation is most unlikely to produce periodic flares, but both the flare mechanisms considered here would naturally follow any periodicity in a source of pumping (or background) radiation.

1.1 Observational Background

At least some flaring variability in astrophysical masers is almost certainly driven by changes in the flux of external pumping radiation incident on a maser zone. The main evidence for this statement comes from correlation between maser flaring events and changes to the flux of infra-red (IR) radiation, from sources close to the maser, that incorporate wavelengths important in the pumping scheme of the relevant molecule. For example, power in the 6.7-GHz maser transition is highly correlated with dust emission at 870 μm (Urquhart et al. 2015). We note that in multi-level systems, IR wavelengths corresponding to individual molecular transitions may cause either an increase or a decrease in maser brightness, depending on the details of the pumping scheme. Variation of the IR pumping radiation has been linked, in at least some massive protostellar sources, to enhanced accretion events (Hunter et al. 2019, 2017). Most of the work described here relates to masers in star-forming regions, but we note that flaring variability in H_2O (Brand et al. 2018) and OH (Etoka & Le Squeren 1997; Etoka et al. 2017) masers has also been observed in evolved stars, in addition to lower amplitude variations linked to the pulsation period, and associated stellar continuum variations, in these sources.

Specific examples of IR/maser flare correlations include the 22-GHz H_2O and 6.7-GHz methanol masers associated with the ucHII region G025.65+1.05 (Sobolev et al. 2019; Stecklum et al. 2017). The H_2O maser variability in this object may be correlated

with IR K-band variability in a source approximately 1500 AU from the maser position (Sobolev et al. 2019). To be precise, the H₂O emission appears to exhibit an anti-correlation, with bright 22-GHz episodes corresponding to times of low K-band (most observations centered on 2.20 μ m wavelength) flux density. This is to be expected for typical 22-GHz masers in star-forming regions, where computational models, for example Gray et al. (2016), show that strong IR emission from dust tends to destroy the 22-GHz inversion, probably by inhibiting the loss of population from the lower maser level (Strelnitskii 1981; Sobolev & Gray 2012). The 6.7-GHz methanol masers in this source have been described as showing a moderate flux rise at the time of a 22-GHz H₂O maser flare (Sugiyama et al. 2017). A radiative mechanism is not the only explanation for H₂O flaring in G025.65+1.05. VLBI observations identify the flaring object with a single compact spot of maser emission (Burns et al. 2020). An image from spectral channels in the blue-shifted wing of this spot shows a double structure, leading to an interpretation as a possible line-of-sight overlap of two masing objects. Preliminary modelling results for spatial overlap (Gray 2018) indicate that this mechanism can produce flares of significantly higher variability index than is typical of radiative pumping mechanisms, and the overlap interpretation therefore becomes more likely if the source is at the further of the two possible distances (2.7 and 12.5 kpc) mentioned in Burns et al. (2020). Another possible example of this overlap mechanism is a very high brightness H₂O flare from Orion KL (Shimoikura et al. 2005). The 22-GHz maser emission of G025.65+1.05 has been monitored by a combination of the Simeiz, Torun and Hartebeesthoek telescopes since 2000 (Vol’vach et al. 2019). Observations were approximately monthly for early data, but on an almost daily basis since a giant flare in 2017-18. During the period 2000-2019, it has flared strongly (peak flux density > 2000 Jy) three times: the peak flux density of each flare shows an increasing trend, whilst the flare duration and inter-flare interval have decreased. The shortest, brightest and most recent flare (2017-18) showed a double-peaked light curve, with rising sections well-approximated by exponentials with characteristic times of approximately 10 d. The exponential shape, backed by evidence from polarization and spectral width, have led Vol’vach et al. (2019) to conclude that the flaring maser is unsaturated. The continuum flux at 870 μ m has generally been rising towards G025.65+1.05 since 2008, but the data is very sparse compared to the maser observations, including an interval of eight years with no data (Vol’vach et al. 2019).

Although correlations between IR radiation and maser flux density have been demonstrated in some sources, observations of the IR radiation have rarely been carried out with sufficiently high cadence to reconstruct accurately the IR light curve associated with a maser flare, though this has been attempted in K-band observations of G025.65+1.05 and G107.298+5.63 (Biszarina et al. 2018). This is just a consequence of the inherent difficulty of observing maser flares: their association with high-mass young stellar objects (YSOs) makes them rather rare and, apart from the known periodic sources, not simply predictable. Perhaps the only case in which a high-cadence (sample separations of hours to weeks) IR light curve has been recorded with the same period (34.6 d) as a flaring maser is that of the intermediate-mass YSO G107.298+5.63, observed with NEOWISE (Stecklum et al. 2018). NEOWISE records in four IR bands, W1-W4, with respective band-centre wavelengths of 3.4, 4.6, 12 and 22 μ m (Nugent et al. 2015). The IR light curve itself has a saw-tooth form, consisting of a steep rise (\sim 5 d) to maximum light, followed by a relatively slow decay that takes approximately 30 d. Possible models for this source are discussed

by Fujisawa et al. (2014). An accretion-pulsation model of a YSO (Inayoshi et al. 2013) would require a much more luminous YSO for the observed period. However, a colliding-wind binary model (van der Walt et al. 2009) was found to agree reasonably well with the maser data. This model has a rapid rise and slow decay, and is therefore also consistent with the IR data from Stecklum et al. (2018). The 34.6 d period is also shared by 22-GHz H₂O masers (Szymczak et al. 2016) that vary in anti-phase with the 6.7-GHz methanol masers discussed above. Their EVN observations were carried out near one peak in the methanol maser emission, and thirteen distinct clouds were detected, in an approximately linear distribution of 400 mas (306 AU) in extent, parallel to a CO outflow.

Another interesting periodic ($P = 243.3$ d) source is G9.62+0.20E, which has correlated flares in transitions of OH and methanol (Goedhart et al. 2019). This was one of the original periodic methanol maser sources monitored by Goedhart et al. (2004). G9.62+0.20E also contains flaring H₂O masers, but these are aperiodic. The particular transitions are the 6.7 and 12.2 GHz transitions of methanol and the 1665 and 1667 MHz transitions of OH. Comparison with VLBI data from Sanna et al. (2015) shows that only a subset of the OH maser spots are involved in the periodic flaring. The shapes and timings of the OH and methanol light curves are different, with the OH transitions exhibiting an initial dip in flux density before rising to peak output. The OH dip appears to coincide with the start of the 12.2-GHz methanol rise, but the OH peaks were delayed with respect to the 12.2-GHz methanol peak by 23 d (1665 MHz) and 13 d (1667 MHz) (Goedhart et al. 2019). These delays are attributed by Goedhart et al. (2019) to a \sim 1600 AU position difference between the OH and methanol maser regions, with the driving mechanism in this source being variation in the free-free background radiation of the masers from a nearby HII region. The periodicity was linked ultimately to colliding-wind binarity. Maser decay from the flare peaks was fitted to a recombination model by van der Walt et al. (2009), but there is currently no measured continuum light curve against which this theory can be tested. An alternative IR driving mechanism, also ultimately dependent on binarity, was suggested by Sanna et al. (2015).

Radiative flare mechanisms have also been suggested for recurrent, but non-periodic, maser flares, such as the multi-species, multi-transition event in NGC 6334I (MacLeod et al. 2018), which was found to be correlated with a sub-mm continuum outburst associated with a rapid rise in dust temperature. Binarity is again discussed by the authors as the likely driver, but in this source the orbit is decaying, leading to progressively shorter inter-flare intervals if the flares are associated with a dust heating event at each periastron. Another source with an IR-methanol maser correlation is S255 NIRS3 (Caratti o Garatti, Cesaroni et al. 2017; Moscadelli et al. 2017). This source is believed to contain a massive protostar of estimated mass $20 M_{\odot}$, that suffered an accretion outburst, visible in the IR, beginning around June 2015. Radiation in the 20-30 μ m waveband is necessary to pump the 6.7-GHz methanol maser (Sobolev et al. 1997). Radiation in this wavelength range appears at pre-outburst and burst levels in the spectral energy distribution shown by Caratti o Garatti, Stecklum et al. (2017), though data at higher spatial resolution were available only in the shorter wavelength IR at the K, K_s and H-bands. A high-cadence light-curve in the K_s band has recently become available (Uchiyama et al. 2019). The source was monitored for 8.5 yr with the Torun 32-m telescope, extended to approximately 23 yr with archival data (Szymczak et al. 2018). Over this time, only modest (20-30%) variability had been noted in the maser flux density prior to the burst of 2015-16. Interferometric (EVN and JVLA) observa-

tions of the associated 6.7-GHz methanol masers (Moscadelli et al. 2017) show that a new flaring cluster of masers formed approximately 1000 AU from NIRS3 in sky projection, whilst a pre-burst maser cluster closer to NIRS3 (~ 400 AU) was destroyed. A minimum propagation speed of $0.02c$ eliminates any shock-wave mechanism for the flare, and requires a radiative link. In common with other sources, the flaring masers occupied a new region in velocity space, whilst other pre-burst spectral features are not affected during the flare. A comparison of single-dish, JVLBA and VLBI data by Szymczak et al. (2018) demonstrates that pre-burst and bursting maser regions in S255 NIRS3 are substantially more extended than the VLBI spots of a few milliarcsec. Moscadelli et al. (2017) estimate the extent of the flaring maser region: 0.24 arcsec, or 430 AU.

If IR pumping radiation always destroys the inversion in a particular transition, as might be supposed for the 22-GHz transition of H_2O if always collisionally pumped, but increases the inversion in another, such as the 6.7-GHz transition of methanol, then it would be possible to distinguish between variable pumping and variable background mechanisms in any source containing these two transitions, if suitably related spatially. A variation in the IR pumping radiation would generally lead to an anti-correlation between the two transitions, whilst a variable background would cause a positive correlation. G107.298+5.63 is an example of the first source type (Szymczak et al. 2016), whilst NGC 6334I (MacLeod et al. 2018) is an example of the second. However, it is not clear that sources can be distinguished unambiguously in this way because the 22-GHz transition is part of a family of H_2O transitions that have both radiative and collisional pumping schemes (Gray et al. 2016). The radiative regime requires, in addition to dust temperatures above 850 K, number densities of about $3 \times 10^{10} \text{ cm}^{-3}$, roughly an order of magnitude higher than the collisional regime, but substantially lower kinetic temperatures of < 300 K (compared to typically 700–1200 K in the collisional regime). Overall, observed anti-correlation between these transitions almost certainly implies a variable IR pumping mechanism, but a positive correlation could arise from either mechanism.

It should also be noted that non-maser explanations exist for flaring molecular line emission. Perhaps the most likely of these is the Dicke superradiance model, see for example Rajabi & Houde (2017). This model relies on the difference between the spontaneous emission characteristics of isolated atoms or molecules, and their behaviour in bulk, where the probability of spontaneous emission depends on a density matrix that represents the statistical properties of a large number of molecules packed into a distance small compared to the wavelength of the emitted radiation.

1.2 Timescales and Cloud Sizes

An important parameter for the modelling work described in this paper is the shortest timescale on which flaring variability occurs (see Section 2.1) and its relation to another important parameter, the linear size of the maser cloud. A useful recent survey in this respect is Shakhvorostova et al. (2018) who monitored seven H_2O maser sources during April–September 2017 with the 22-m Simeiz telescope at an approximately monthly cadence. All these sources exhibited variability, and very large flux density changes were recorded on the shortest spacings between observations (20–30 d). Size estimates from related interferometric observations in two of the sources returned maser spot sizes of ~ 2 AU in G34.403+0.233 (Kurayama et al. 2011) and 2.7 AU in G43.80.13 from 2015 RadioAstron data. These spot sizes can possibly be regarded as typical, but neither can be directly identified with the flaring objects. In

the case of the object with the known high-cadence IR light curve, G107.298+5.63, a parallax distance of 750 ± 27 pc was calculated by Hirota et al. (2008) so 1 mas in this source corresponds to a linear distance of 0.75 AU. Figures in Hirota et al. (2008) that show individual H_2O maser spots are therefore consistent with diameters of ~ 2 AU. No sizes were available for the methanol masers in this source, but the periodic source, G9.62+0.20E, was imaged with the VLBA in the 12.2-GHz methanol maser line by Goedhart et al. (2005). These 12.2-GHz observations detected 16 components, correlated in position and Doppler velocity, with compact core sizes of ~ 2 mas. However, G9.62+0.20E is at 5.7 kpc, so the linear sizes of methanol maser clouds could be significantly larger (of order 10 AU) than those supporting H_2O masers. Analysis of the detected components showed no abrupt motion changes, or appearance of new components, again suggesting a radiative driving mechanism, rather than, for example, a shock impact.

Measured VLBI spot sizes may give a poor estimate of the extent of the physical object through which a maser amplifies unless the observation includes short baselines. Estimates from Moscadelli et al. (2017) for the typical sizes of 6.7-GHz methanol maser spots are 2–20 AU for compact cores, with haloes of weaker emission extending 10–300 AU. The much larger extent (430 AU) of the flaring emission in S255 NIRS3 is probably not problematic, since this maser appeared to be unsaturated, yielding a light-crossing time, for the maser radiation, of $\simeq 2.4$ d. Overall, < 1 AU-scale clouds are probably typical for H_2O masers, based on clustering scales from Uscanga et al. (2010), but sizes an order of magnitude larger are likely typical for methanol (2–30 AU), based on measurements in 13 sources (Sugiyama et al. 2008) while larger-scale structures cannot be ruled out. In Cepheus A, Uscanga et al. (2010) find a clustering scale of 0.31 ± 0.07 AU for H_2O masers. In the same source, methanol 6.7-GHz features from Torstensson et al. (2011) have a scale of ~ 5 milliarcsec (3.5 AU) which is consistent with the methanol clouds being systematically larger.

1.3 Flare Mechanisms

In this work, we are primarily concerned with the detailed response of a maser cloud to a known driving light curve for pumping or background radiation, under a range of possible levels of saturation, and the variation of the response with the viewing direction of the observer. We are less concerned with the physical mechanism, involving a binary system or otherwise, that produces the pumping radiation, unless the theory is sufficiently developed to predict the functional form of the light curve. The observational IR light curve from G107.298+5.63 (Stecklum et al. 2018) is particularly useful in this respect.

A brief, but almost certainly not complete, survey of known flare pumping models, from the early stellar wind compression model by Strelitskii (1982) to the very recent schemes listed in Goedhart et al. (2019), suggests that none of these authors themselves make detailed predictions of the expected IR light curve. The bipolar outflow model by Singh & Deshpande (2012) includes predicted periodic maser light curves, but it is not clear how these relate to the pumping radiation. Interestingly, these curves mostly show a slow rise and rapid decay of the maser, and so would not obviously follow from the observed IR light curve in Stecklum et al. (2018).

Flare-driving models have been compared (van der Walt et al. 2016) with respect to their ability to reproduce a periodic methanol maser light curve similar to that found in G9.62+0.20E. To make this comparison, van der Walt et al. (2016) require light curves for

pumping or background radiation. They argue that the accretion-pulsation model (Inayoshi et al. 2013; Sanna et al. 2015) should have a light curve in the pumping radiation that is qualitatively similar to a pulsating variable, for example a Cepheid, since the pulsation is controlled by a similar opacity mechanism. Light curves for the rotating spiral shock model by Parfenov & Sobolev (2014) were calculated by van der Walt et al. (2016) for the cases of the stars alone, for the trailing shock, and the combination of these. The trailing shock case looks qualitatively like the maser light curves from Singh & Deshpande (2012): slow rise and rapid decay.

The model by van der Walt (2011) is different in that it produces the maser flare via temporal change in the background radiation at the maser frequency, rather than the IR pumping radiation. A model of similar type has been used to explain the first known periodic H₂CO maser (Araya et al. 2010). A binary protostellar source is required with a colliding wind structure, and considerable eccentricity. With the aid of additional formulae in van der Walt et al. (2009), there is enough information to reconstruct the light-curve of the background radiation. Periodic 6.7-GHz methanol masers appear to have several different forms for the light-curve, for example Szymczak et al. (2015), with the likely implication that the same is true of the light curves of the pumping or background radiation.

2 MODELLING CONSIDERATIONS

The present work approximates a fully time-dependent problem by a time-series of time-independent solutions. There is therefore some timescale, for a given cloud, below which the method becomes rather poor. The details relating to this timescale are discussed first, in Section 2.1. In Sections 2.2-2.5, we discuss additional important considerations related to the internal structure of the source and the representation of the pumping models for external pumping radiation and background intensity.

The code used in the present work is closely based on that used in Paper 1 and Paper 2. The main modification in the present work is a new capability to model clouds that are non-uniform in the unsaturated inversion. This may be interpreted as either a cloud of constant density with a variable pump rate, or constant pump rate within a cloud of variable density. Clouds considered in this work either have uniform physical conditions, or have an unsaturated inversion profile, $\delta \propto 1/r^2$, where r is the radius drawn from the coordinate origin at the approximate centre of the cloud. This dependence remains radial, even for clouds with a non-zero deformation factor, Γ . As in Paper 2, node distributions followed the shaping equation,

$$(x^2 + y^2)e^\Gamma + z^2e^{-2\Gamma} = 1, \quad (1)$$

where (x, y, z) are Cartesian coordinates, such that $\Gamma < 0$ ($\Gamma > 0$) yields an oblate (prolate) cloud.

2.1 Applicable Timescales

A series of time-independent models is a good approximation to a time-dependent solution provided that steady-state radiative transfer can be established on a time scale that is much shorter than any timescale related to the maser pump. If the pumping scheme is radiatively dominated, this corresponds to a timescale associated with the variation of an external radiation source (either for the background or the pumping radiation). We establish a link between the flux of pumping radiation and the optical depth multiplier of the cloud in Section 2.3, so that we may use a time-series of models

of the same domain, but at different values of the depth multiplier, provided that the evolution of that multiplier (or its proxy, the pump rate) is suitably slow.

The most optimistic, or shortest, timescale on which steady state radiative transfer might be established is the light crossing time of the cloud. For a cloud of radius r_{AU} astronomical units, this minimum time is $t_{lc} = 1000r_{AU}$ s. If the entire pumping scheme relies only on transitions of modest optical depth, τ_p , say up to order ~ 1 , it is a reasonable approximation to use t_{lc} , and the minimum representable timescale of a time-series model will be no more than a few hours for maser clouds of reasonable size.

We should, however, increase the minimum representable timescale to something considerably larger than t_{lc} on the following grounds. Firstly, the depth-multipliers of the maser transition itself in the model take values up to 35: certainly not a modest depth. In the two-level approximation, the pumping radiation is also linked to this single transition. However, in a multi-level model of a real molecule, a complex pumping scheme might depend on transitions of even larger optical depth - perhaps running up to values in the thousands. For example, the $5_{2,3}$ down to $4_{1,4}$ transition of o-H₂O at 53.1 μ m has an optical depth of 5267 under conditions corresponding to the largest 22-GHz inversion ($T_{kin}=766$ K and $n_{H_2}=6.7 \times 10^9$ cm⁻³) found in the parameter-space search modelling by Gray et al. (2016). This transition plays an important role in the classic ‘collisional’ pumping scheme for the 22-GHz maser (de Jong 1973; Gray 2012). The geometry used in Gray et al. (2016) is different from the current work, and the clouds in that work have a scale size of 15 AU. However, optical depths of 350-1000 in the $5_{2,3} - 4_{1,4}$ line might still be considered reasonable for clouds considered typical in the present work.

In such a pumping scheme, a diffusion solution is appropriate for a transition of very high optical depth, and then the minimum representable time becomes the photon diffusion time of order $\tau_p t_{lc}$, that is our original light crossing time multiplied by the optical depth in the pumping line. In this case, minimum representable timescales of 12 d apply for a 1 AU radius cloud and 60 d for a 5 AU radius cloud if a pumping scheme is controlled by a transition with an optical depth of 1000. Such timescales certainly impinge on the more rapid observed maser flares with rise times of order weeks to months.

However, even if very optically thick transitions are important in a pumping scheme, the situation is likely to be rather more optimistic than the estimates for a depth-1000 line calculated above. The reason is the concept of effective scattering, quantified through the scattering parameter. In the two-level case this is

$$\zeta = \frac{\Delta C_{u,l}}{\Delta C_{u,l} + g_u A_{u,l}}, \quad (2)$$

where $\Delta C_{u,l}$ is the nett downward collisional rate in the transition between lower level l and upper level u , with statistical weight, g_u . The transition has a spontaneous emission rate controlled by $A_{u,l}$, its Einstein A-coefficient. Effective scattering describes a situation where a photon is formally absorbed in a transition, but there is a high probability that a replacement photon will be spontaneously emitted into the same transition before the energy of the original photon can be thermalized amongst the energy levels and thermal motions of the molecules. Effective scattering then corresponds to the case where $A_{u,l}$ dominates over the collisional rate and ζ , from eq.(2), is small. Effective scattering reduces the optical depth from τ_p to the effective value of $\sqrt{3\zeta}\tau_p$. This effective value is often significantly smaller than the value based simply on the absorption coefficient. For example, for some optically thick

119- μm transitions in OH, the $\sqrt{3\zeta}$ factor is 0.032 (Gray 2007). We note that a transition that has high depth owing to a large A-value will, for the same reason, likely have a small ζ . Another useful example is the 45.1- μm pumping transition in ortho- H_2O that supports inversion at 22 GHz. The 45.1- μm transition has an Einstein A-value of 0.4205 Hz, and an upper level statistical weight of $g_u = 11$. Under conditions close to those for maximum maser depth (see Fig. 5 of Gray et al. (2016)) the second-order downward collisional rate coefficient is approximately $8.9 \times 10^{-12} \text{ cm}^3 \text{ s}^{-1}$. The corresponding first-order collisional coefficient, at an H_2 number density of $6.7 \times 10^9 \text{ cm}^{-3}$, is 0.06 Hz. The net rate, $\Delta C_{u,l}$ in eq.(2) will be smaller. In fact, using $T_{\text{kin}} = 750 \text{ K}$, the upward rate coefficient is 0.0474 Hz, yielding the nett downward value of 0.012 Hz. The value of ζ for the 45.1- μm transition from eq.(2) is therefore 0.0026, yielding $\sqrt{3\zeta} = 0.088$. This transition therefore also has rather strong effective scattering, though not to the same extent as the OH transition.

We suggest, given the examples above, that an order of magnitude reduction in the optically thick timescales may be recovered on the basis of strong effective scattering in very thick pumping lines, so that better estimates for the minimum representable timescales for the model used in the present work are of order $1.2 r_{\text{AU}} \text{ d}$.

In the case of variable background radiation, the limiting timescale is the light-crossing time multiplied by the optical depth in the maser transition itself. The thickest models considered have maser optical depths of 35 so, using the formula for the light-crossing time above, the minimum representable timescale for variable background models is $35000 r_{\text{AU}} \text{ s}$, or 0.4 d for a 1 AU cloud. Somewhat shorter timescales are therefore representable in variable background models.

2.2 Clouds with Variable Unsaturated Inversion

The non-linear algebraic equations used to derive nodal solutions for the inversion were derived in Paper 1. The specific equation incorporating the finite-element discretization used for computations is eq.(24) of that work. In the case of internal variability, one cannot scale all nodal inversions by a single unsaturated value, so eq.(3) of Paper 1 becomes incorrect. We write instead a version in terms of absolute inversions, $\Delta(\mathbf{r})$, with unsaturated values, $\Delta_0(\mathbf{r})$, that can now vary with position, \mathbf{r} . This more general form of Paper 1, eq.(3), is $\Delta(\mathbf{r}) = \Delta_0(\mathbf{r})/[1 + \bar{j}(\mathbf{r})]$. We now divide this expression by the maximum unsaturated inversion in the model, so that the left-hand side becomes $\Delta(\mathbf{r})/\Delta_{0,\text{max}} = \delta(\mathbf{r})$. A similar operation on the right-hand side leaves

$$\delta(\mathbf{r}) = \delta_0(\mathbf{r})/[1 + \bar{j}(\mathbf{r})]. \quad (3)$$

Providing this new scaling is also applied to the gain coefficient in the radiation transfer part of the problem, with a consequent change in the optical depth scale, eq.(24) of Paper 1 takes the form,

$$\delta_i - \delta_{0,i} \left[1 + \frac{i_{BG}}{4\pi} \sum_{q'=1}^{Q'} \frac{a_{q'}}{s_{q'}^2} \sum_{n=0}^{\infty} \frac{1}{n!(n+1)^{1/2}} \left(\sum_{j=1}^J \Phi_{j,q'} \delta_j \right)^n \right]^{-1} = 0, \quad (4)$$

noting that the only formal modification is $\delta_{0,i}$, the scaled unsaturated inversion at node i , multiplying the square-bracketed term. In eq.(4), inversions at general position \mathbf{r} have been replaced by discretized versions specific to a node, indicated by a subscript. We now apply a second, node-dependent, scaling to eq.(4) by dividing throughout by $\delta_{0,i}$. New fractional inversions $\delta'_i = \delta_i/\delta_{0,i}$ are

now guaranteed to take values between 0 and 1, and are the variables solved for computationally. The slightly modified final form of eq.(4) is

$$\delta'_i - \left[1 + \frac{i_{BG}}{4\pi} \sum_{q'=1}^{Q'} \frac{a_{q'}}{s_{q'}^2} \sum_{n=0}^{\infty} \frac{1}{n!(n+1)^{1/2}} \left(\sum_{j=1}^J \delta_{0,j} \Phi_{j,q'} \delta'_j \right)^n \right]^{-1} = 0. \quad (5)$$

Equation 5 shows that the same set of pre-computed saturation coefficients used in Papers 1 and 2, the $\Phi_{j,q'}$, can be used with variable unsaturated inversion too, provided that each coefficient is multiplied by the appropriate scaled unsaturated inversion.

A further computational note is that eq.(5) has an optical depth scale based on the maximum nodal unsaturated inversion in the model. This scaling is rather thick compared to the typical behaviour of a uniform cloud. It is computationally convenient to have global optical depth multipliers that give approximately similar levels of saturation for an internally variable cloud and one with uniform unsaturated inversions. A multiplicative bias is therefore applied to the depth scale. In the present work, this was the mean of the scaled nodal unsaturated inversions. However, this might not be appropriate for all internal variability functions, and we prefer scaling by the maximum unsaturated inversion, and the adoption of a separate bias, to a default scaling by the mean unsaturated inversion.

2.3 Notes on Pumping Variability

In a two-level model of the type used in the present work, varying the pump rate of the maser (or to be more precise, the ratio of the pump rate to the loss rate) is equivalent to varying the optical depth of the model. This assertion is justified as follows: Variation in the pump rate changes the unsaturated inversion. As we have seen in Section 2.2 above, the unsaturated inversion controls the optical depth scale. In a uniform model, this will be via a global multiplier; in an internally variable model, there will be a global multiplier that is in turn multiplied by a node-dependent unsaturated inversion. Overall, however, a time variable pump rate corresponds to a time-variable depth multiplier.

Computationally, the conclusion from the paragraph above is vital: a sequence of solutions, for a particular computational domain, at a number of different values of the depth multiplier can be used to represent a sequence of snapshots in time with different values of the pump rate. There are some provisos to this conclusion. The most important proviso is that the time-dependence of the pump rate is slow compared to any processes, including radiative transfer, within the cloud (or domain). This point is discussed in more detail in terms of the minimum representable timescale in Section 2.1. A second proviso is that a suitable function can be found to represent the time dependence, preferably with observational constraint. Once a suitable function has been selected, inversions at all nodes of the domain can be generated as a smooth function of time (as a proxy for depth multiplier) via interpolation.

2.4 Internal Variability of the Pump

Whilst it is true that the inversion at any node is proportional to its local pump rate, and the pump rate is proportional to the optical depth multiplier of the model, as justified in Section 2.3, it is not trivial to justify extending this proportionality all the way to the energy density of infra-red radiation provided by a protostar or

other source. For some key pumping transition, the pump rate will be proportional to the mean intensity in that transition at the node. However, that local mean intensity is not trivially linked to what might be incident on the surface of the cloud.

We have introduced, in Section 2.1, the idea of an optically thick pumping line in the effective scattering approximation. Solution of the radiation diffusion equation in this limit yields an expression for the mean intensity at a node where the pumping line depth is τ_p :

$$\bar{J}(\tau_p) = \bar{J}(0)e^{-\sqrt{3\zeta}\tau_p} + B_\nu(T_K), \quad (6)$$

where $\bar{J}(0)$ is the surface mean intensity that follows the driving light curve, and T_K is the kinetic temperature local to the node.

We suggest that the two cloud types used in this work should have the following interpretations: The clouds with uniform unsaturated inversions should be interpreted as clouds with a realistic density profile, that rises towards the cloud centre, but is compensated by a falling energy density of pumping radiation, predicted by eq.(6). Obviously this is only an approximation, since the functional forms for the physical density and the energy density of pumping radiation are most unlikely to compensate each other exactly. In this interpretation, The internally uniform clouds represent a thicker regime in respect of the pumping radiation, where $\sqrt{3\zeta}\tau_p$ can rise to perhaps 5-10, and τ_p can be much larger. The second type of cloud, with variable unsaturated inversion, should be interpreted again as a cloud with a centrally condensed density profile, but where we now assume that the first term in eq.(6) dominates the pumping. This implies that the effective optical depth in the pumping line must be small, even if τ_p is substantial. The internally variable clouds therefore correspond to the case of optically thinner pumping lines, where $\sqrt{3\zeta}\tau_p$ is small.

2.5 Notes on Background Variability

The specific intensity of the background radiation, i_{BG} , amplified by the maser is a parameter that appears in eq.(5). Therefore, provided this parameter varies slowly compared to the minimum representable timescale for the cloud, we may adopt a time-series procedure similar to that used for variation in the pumping radiation, but we now use a series of models with different background intensities to study the light curve, rather than models with different depth multipliers. The depth multiplier is generally kept constant in models where the background varies. In the present work, the background specific intensity is considered to be uniform over solid angle. This flare mechanism has been introduced by van der Walt (2011); van der Walt et al. (2016). However, it is an unlikely explanation for the periodic G107.298+5.63 system, since a variable background would be expected to produce correlated H₂O 22 GHz and methanol 6.7 GHz emission, rather than the observed anti-correlation that strongly favours a variable pumping explanation (Szymczak et al. 2016).

3 DOMAINS

In order to cover a reasonable range of models, we considered three standard domains with deformation factors of $\Gamma = -0.6, 0.0, +0.6$ corresponding, respectively, to models that are substantially oblate, quasi-spherical and substantially prolate. As in Paper 2, deformations were applied to originally spherical point distributions via eq.(1). Views of the two domains with $\Gamma \neq 0$ appear in Fig. 1 of Paper 2, and a somewhat smaller quasi-spherical domain appears

in Fig. 1 of Paper 1. We do not repeat plots of the domain structure here.

All three domains may be presented in the form with internally uniform conditions, and in a version where unsaturated inversions, $\delta_{0,i}$, at the nodal points follow the formula

$$\delta_{0,i} = \delta_{out}(r_i/r_{out})^{-2}, \quad (7)$$

where $\delta_{out} = 1.0$ is the unsaturated inversion at the node with the largest radius, r_{out} , measured from the origin of the domain. The variable unsaturated inversion models were designed to produce a core-halo structure that is common in many observed masers at VLBI resolution. The extent to which this was successful or not may be judged from the results in Section 4. The number of nodes per domain was similar to those used in Paper 2, with approximately 250 of an original list of 300 nodes surviving the triangulation process.

The same ray-tracing algorithm was used here as in Paper 1 and Paper 2, so that solutions for the inversions involved tracing 1442 rays from points on a celestial sphere-style source to each target node of the domain. The celestial sphere source had a standard specific intensity of $i_{BG} = 1.0 \times 10^{-6}$, in cases where the maser pump was varied, and a range of 10^{-9} to 10^{-5} in the case of a variable background, where $i_{BG} = I_{BG}/I_{sat}$, and I_{sat} is the saturation intensity of the maser. The upper limit of the variable background corresponds to the background intensity used in Paper 1 and Paper 2. The background and pumping radiation is taken to be isotropic in all cases.

4 RESULTS

First, in Section 4.1, we introduce the functional forms that we will use as models for the light curves of pumping and background radiation, before briefly demonstrating the main effects of changing the model from one with uniform physical conditions, to one with variable unsaturated inversions (Section 4.2).

The main results, in the form of formal radiative transfer solutions, seen as images and spectra by an observer, appear in Section 4.3 and Section 4.4, where we discuss, respectively, the effects of pumping and background radiation on the maser, in terms of saturation, cloud shape and the observer's viewpoint. This work is extended to a consideration of light curves with statistical information in Section 5.

4.1 Input Light Curves

In the rest of this work, we use the following driving light curves to represent the time variation of either the pumping or background radiation: function D_0 is a default sinusoid, $1 + \sin(x)$; function D_1 is a digitized version of the observed IR light curve from the work of Stecklum et al. (2018); function D_2 is a theoretical Cepheid variable light curve from the top left panel of Figure 1 from Bhardwaj et al. (2017), and is used to represent the accretion-pulsation model, following the suggestion of van der Walt et al. (2016); functions D_3 - D_5 are respective digitized forms of the light curves used by van der Walt et al. (2016) to represent pumping by the stars alone, by the trailing shock and by the sum of these sources following the spiral shock model by Parfenov & Sobolev (2014). In a little more detail, this model consists of a primary and secondary star in a circular binary orbit within a circumbinary disc. The primary has a trailing shock that heats gas and dust (see Fig. 2

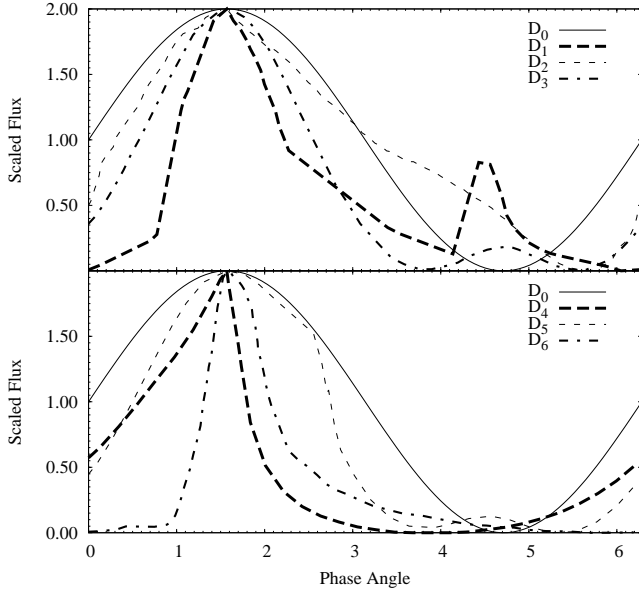


Figure 1. Driving functions used in the flare modelling in later sections. The top panel shows functions $D_1 - D_3$ (see text) compared to the default sinusoid, $1 + \sin(x)$, as D_0 . The lower panel compares D_0 with driving functions $D_4 - D_6$. All functions are scaled to an amplitude of 1 with the maximum occurring at $\pi/2$ radians.

of van der Walt et al. 2016). The light curve follows the illumination of a point on the inner edge of the circumbinary disc by the stars, the shocked material, or both of these sources. Finally, function D_6 is the light curve for background radiation predicted by the colliding-wind eccentric binary model. The decay is constructed from equations in van der Walt et al. (2009), but the rise has been modelled by a simple exponential, as van der Walt et al. (2009) do not provide a functional form for this part of the light curve. The recently published light curve from Uchiyama et al. (2019) is discussed briefly in Section 9.

All the functions, $D_0 - D_6$, are drawn in Fig. 1 with equal y -axis range and with maximum light at a phase of $\pi/2$. Where functions have been digitized, this process was carried out with the WebPlotDigitizer tool, by Ankit Rohatgi¹. Where necessary, continuous functions were reconstructed from the digitized data via a cubic splining process, based on the functions SPLINE and SPLINT (Press et al. 1992). The original Cepheid light curve was presented with a y -axis in magnitudes, and this curve has been re-plotted here on a linear scale. In this work, we do not specify a particular functional form for the IR light-curve of a source of the accretion-burst type, for example S255 NIRS3, on the grounds that present data are too sparse to generate anything that might be regarded as typical.

4.2 Nodal Solutions

Nodal solutions were generated in a broadly similar manner to those in Paper 1 and Paper 2. The interesting point in the present work is that the sequence of solutions at increasing optical depth now represent different levels of pumping radiation, and therefore potentially correspond to different times in a radiation-driven pumping cycle. To limit the overall complexity of the parameter space, we restrict the domains used in the present work to one

oblate, one prolate and one spherical domain. These have the respective deformation factors -0.6, 0.6 and 0.0 from eq.(1). To allow us also to model the effects of a variable background, several sets of solutions were generated with background levels, in saturation units, ranging from 10^{-9} - 10^{-5} for the prolate and oblate clouds.

All solutions in the present work were computed using the non-linear Orthomin(K) algorithm (Chen & Cai 2001), with the order $K = 2$. For each domain considered, solutions were computed for optical depth multipliers of 0.1 to at least 30.0 in steps of 0.1. All solutions assumed complete velocity redistribution, and we note that the levels of saturation reached for the highest depth multipliers ($\tau \sim 30.0$), corresponding to actual maser optical depths of order 60 on some lines of sight, are almost certainly at the upper limits of the validity of this approximation, even for rapid redistribution mediated by the pumping radiation (Frisch 1988; Field et al. 1994; Gray 2012).

To demonstrate the difference between the uniform and internally variable clouds, we show in Fig. 2 images and spectra of both cloud styles for the oblate domain, viewed edge on, together with histograms that show the level of saturation in the model through the occupancy of bins that represent remaining fractional inversion. Both examples have a moderate optical depth multiplier of $\tau = 15.0$, and were amplified from a background of $i_{BG} = 10^{-5}$.

The internally variable clouds are perhaps a reasonable representation of a core-halo structure that is sometimes present in 6.7-GHz methanol maser sources. From Fig. 2, the outstanding features of adopting a cloud with variable unsaturated inversion, weighted such that inversions are highest towards the centre, is to reduce the angular size of the brightest region of the image. The spectrum is narrower, but has a lower flux density, than the uniform case. The saturation profile is significantly different too: the uniform cloud is arguably more highly saturated generally, with more nodes in the 0.1 – 0.2 inversion bin than in any other. However, the internally variable cloud has a significant population in the most saturated bin 0.0 – 0.1 of the original inversion remaining, whilst this bin is empty in the uniform case.

4.3 Variable Pumping Radiation

We begin by studying the effect of saturation by applying functions $D_0 - D_5$ to represent the time-series in optical depth multiplier, as a proxy for the maser pump rate, as discussed in Section 2.3, with the caveats raised in Section 2.4. These functions were applied in the form,

$$\tau(t) = \tau_{min} + (1/2)\Delta\tau D_n(t), \quad (8)$$

where $\Delta\tau = \tau_{max} - \tau_{min}$, and τ_{min} (τ_{max}) is the optical depth multiplier of the thinnest (thickest) nodal solution employed, and n is in the range 0-5. Apart from the function index, n , there are two parameters in eq.(8): the minimum optical depth multiplier, τ_{min} , and the multiplier range, $\Delta\tau$. Suitable values of these parameters should be informed by observation and available data. The multiplier range is perhaps the easier parameter to constrain via the original y -axis ranges of functions $D_1 - D_5$. Excluding function D_2 , where the original data is in magnitudes, leading to a flux ratio (of 1.629), the remaining functions have changes in the flux of pumping radiation ranging from 0.94 (D_4) to 3.22 (D_1). As these changes are proportional to changes in the optical depth scale of the domain, it is reasonable to set these, or the rounded figures of 0.9-3.5 as the bounds of $\Delta\tau$. Given that the longest maser gain lengths in a scaled cloud are closer to 2 than 1 (diameter rather than radius) then if the amplification is entirely unsaturated, these

¹ <https://automeris.io/WebPlotDigitizer>

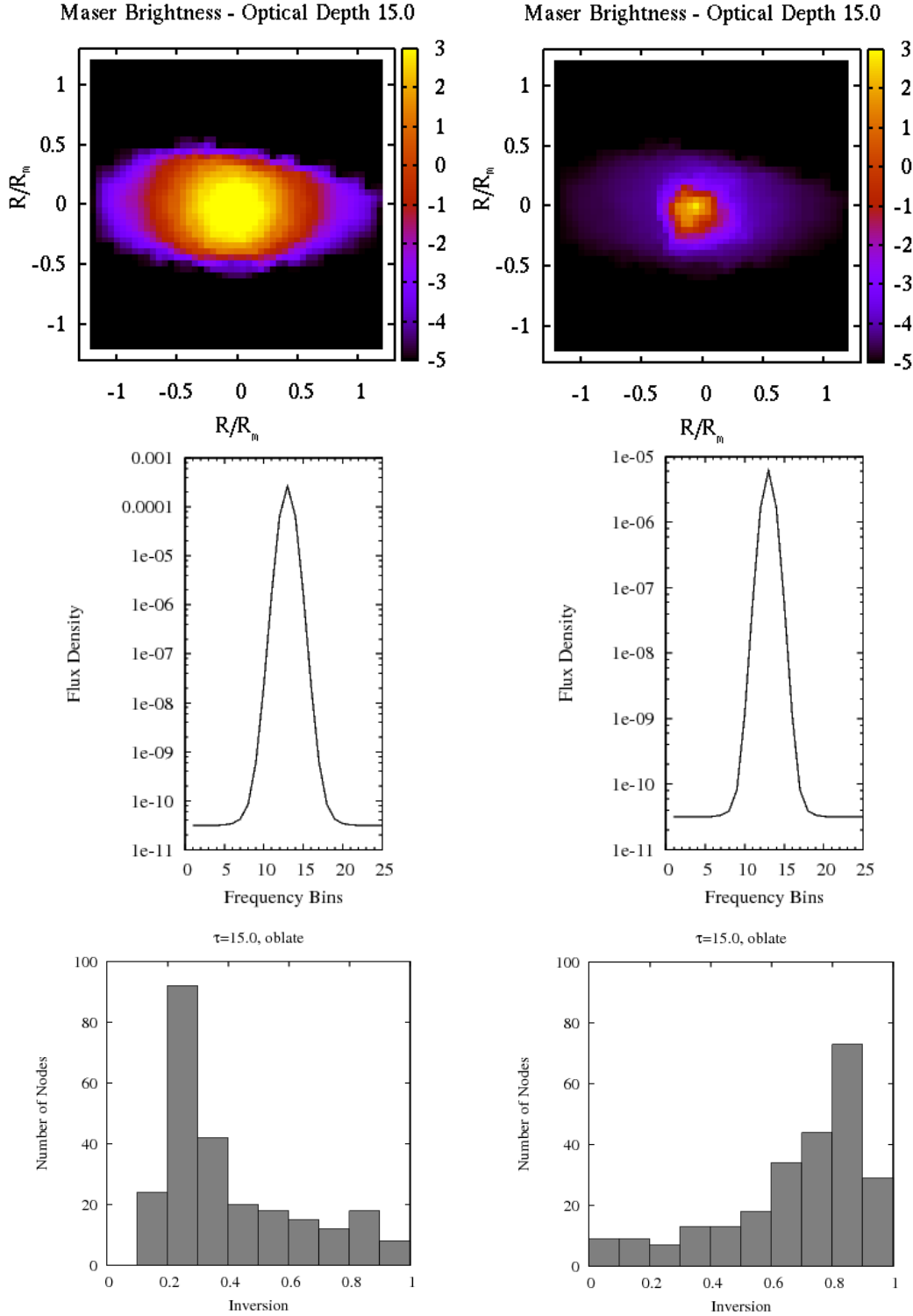


Figure 2. Images, spectra and saturation histograms for $\Gamma = -0.6$ oblate clouds with uniform conditions (left-hand column) and a $1/r^2$ profile of the unsaturated inversion (right-hand column). Both datasets use the same geometric distribution of nodes. The spectra and maps are as viewed by an observer at polar angle = azimuthal angle = $\pi/2$.

figures would lead to maser intensity ratios between maximum and minimum light, along a given line of sight, of 6.05 and 1100. These figures are perhaps a poor guide anyway, as there are no light curves available at the wavelength range that is known to be important for pumping. We typically used $\Delta\tau = 5.0$, and occasionally larger

figures on the grounds that observed maser flares are known with variability indices considerably in excess of 1000.

For each model, two formal solutions were computed for every nodal solution, or optical depth multiplier, available. The first of these places the observer close to the optimum viewing posi-

tion for the prolate and oblate clouds. The second uses a randomly chosen viewpoint. The reason for choosing the first type is that observations are obviously biased towards the detection of the brightest masers, so we are quite likely to be observing objects close to optimally oriented to our line of sight. The second type of formal solution gives us an idea of the sort of flare that might result from an average cloud, selected from an ensemble of similar objects.

Light curves were constructed by taking one of the observable parameters from the formal solutions and computing its response to the driving in depth from eq.(8). In detail, this was carried out by fitting a cubic natural spline through the parameter values at the known depths.

4.4 Variable Background Radiation

The operations for variation of the background radiation follow a broadly similar approach to those used in Section 4.3. However, there are important differences. Firstly, we apply only the default sinusoid and function D_6 as driving functions, since only D_6 is based on a model where the background, rather than the pump, is varied. The process is easier in the sense that the parameter that is varying in time is simply a parameter in eq.(4), and no complicated justification is required for its use. A significant complication in the variable background case, however, is that the driver in the background analogue of eq.(8)

$$i_{BG}(t) = i_{BG,min} + (1/2)\Delta i_{BG} D_6(t), \quad (9)$$

now demands a response from a number of different models, each computed with a different value of i_{BG} . Therefore, modelling flares from background variation is computationally considerably more expensive.

5 VARIABLE PUMPING RESULTS

We plot, in Fig. 3, the flare light curves, over one period, that result from driving with pump functions $D_0 - D_5$ for a prolate cloud with $\Gamma = 0.6$, with the observer placed in the optimum position (viewing the cloud along the z -axis close to the long axis of the cloud). The cloud style is uniform in unsaturated inversion. The parameters of eq.(8) in this case are $\tau_{min} = 10.0$ and $\Delta\tau = 5.0$, corresponding to a regime that is already characteristic of quite strong saturation. Throughout Section 5, the y axes of graphs are shown in flux density, based on a background specific intensity that is scaled to the saturation intensity of the maser transition. Flux density is likely the best parameter to plot in view of the prominent role of single-dish monitoring in repetitive flare studies. An explanation of the flux-density scale appears in Appendix A. Owing to the nature of the saturation intensity, and particularly the fact that this quantity may itself depend on the energy density of pumping radiation, a conversion formula to units of Jy at a typical source distance, and for a particular maser transition, for example, is not trivial. Such a conversion is also discussed in detail in Appendix A. The variability index of the maser light curve, defined as in the Introduction as F_{pk}/F_{qui} is 1.74 in Fig. 3. The same parameter for the driving functions, replacing flux densities with values of the depth multiplier, is 1.5. Although the variability index of the maser is significantly larger here, the light curve in Fig. 3 demonstrates the smoothing effect of saturation: as exponential growth gives way to a functional form that is closer to linear at high flux density, the maser responds more weakly to the driving function, smoothing particularly the high flux density parts of the light curves. Note that,

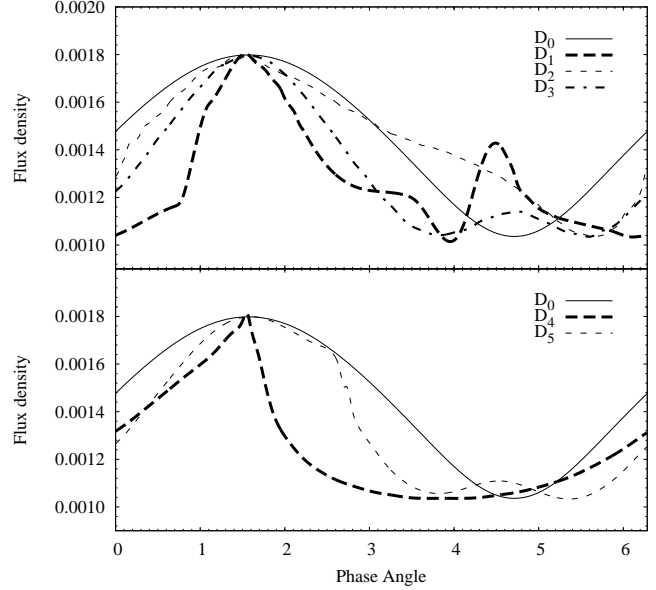


Figure 3. Maser light curves resulting from driving functions D_0 to D_3 (upper panel and D_4 , D_5 with D_0 (lower panel) applied to a $\Gamma = 0.6$ prolate cloud. Optical depth multipliers in this model ranged from 10.0 to 15.0. The observer is in the optimum viewing position.

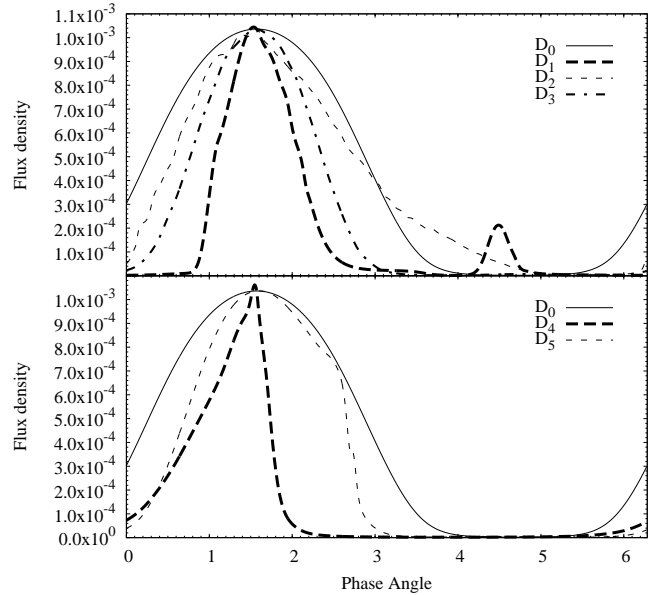


Figure 4. As for Fig. 3 but with an optical depth multiplier range of 5.0 to 10.0.

compared to Fig. 1, secondary features at low flux density, such as the small peak in function D_1 , are exaggerated.

Fig. 4 depicts a scenario where growth is less saturated. Again the amplitude in depth parameter is 5.0, but now the optical depth range lower and upper limits are 5.0 and 10.0, respectively, so that the upper limit flux density here corresponds to the lower limit in Fig. 3. The variability index of the flare in Fig. 4 is 502, compared with 1.74 in Fig. 3. The weaker parts of the light curve are now compressed down to the x -axis, and the duty cycle, defined as the fraction of the period over which the light curve is above the mean of its maximum and minimum values, is reduced compared to the driving functions.

As a last example of the effects of saturation, we show in Fig. 5

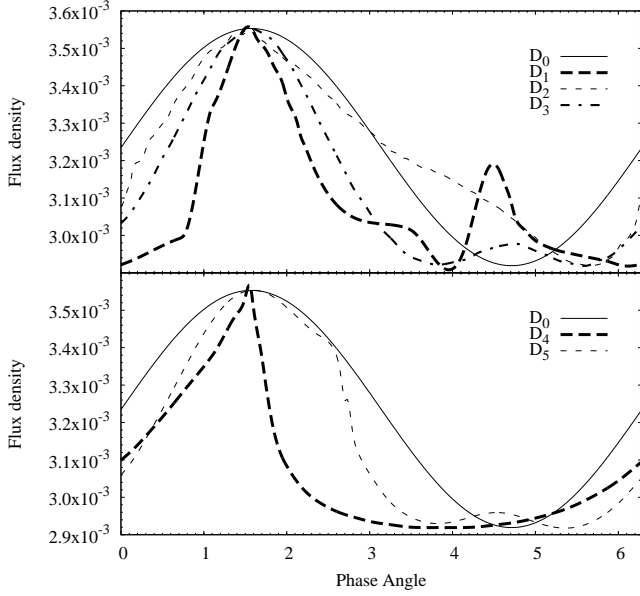


Figure 5. As for Fig. 3 but with an optical depth multiplier range of 24.0 to 29.0.

a situation with the same amplitude in depth (or mean intensity of pumping radiation) of 5.0, but with a minimum depth multiplier of 24.0, corresponding to extreme saturation in the context of this model. The compression of the response is more extreme than in Fig. 3, with a variability index of the ‘flare’ now only 1.22 (compared to 1.208 for the driving functions). In terms of shape, the curves in Fig. 5 more strongly resemble the driving functions plotted in Fig. 1 than the case of moderate saturation in Fig. 3, where the high flux density parts of the response are broadened, or of the weak saturation case of Fig. 4, where the high flux density parts of the response are narrowed in a high variability index flare. This behaviour is in accord with the linear gain expected of highly saturated masers.

5.1 Effect of Viewpoint

In this section, the observer’s viewpoint is moved to a ‘typical’ position instead of the view close to the long-axis of the domain. In spherical polar coordinates, the chosen position has polar angle of 1.081 radian, and an azimuthal angle of 3.465 radian. Light curves that result from a driving range in depth from 5.0-10.0, analogous to Fig. 4, are plotted in Fig. 6. We defer a discussion of the statistics related to a large number of random viewpoints until Section 7. The effect of moving away from the optimum viewpoint is highly significant. The variability index in Fig. 6 is 580, as opposed to 502 in Fig. 4, indicating reduced saturation. However, the shapes of the light curves indicate this more visually: there is no broadening of the curves in the higher flux density regime, indicating little saturation even at the highest flux densities attained in Fig. 6. A glance at the y axis shows that the highest flux density attained is only 2.28×10^{-7} , a factor of 4600 below that obtained in the optimum orientation, and in fact almost an order of magnitude below the minimum achieved in Fig. 4.

5.2 Extreme Flares

From the work in Section 5 so far, it is clear that the way to get a high amplitude flare from variable IR pumping is to introduce a

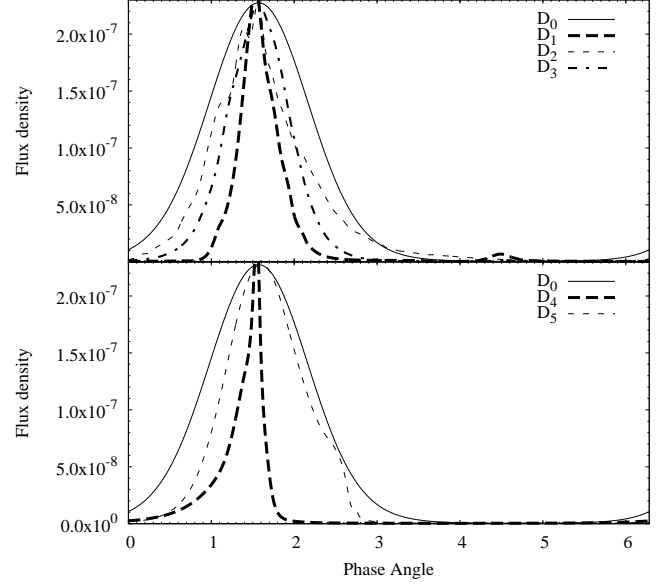


Figure 6. As for Fig. 4 but with the observer’s viewpoint shifted to $(\theta, \phi) = (1.081, 3.465)$ radians.

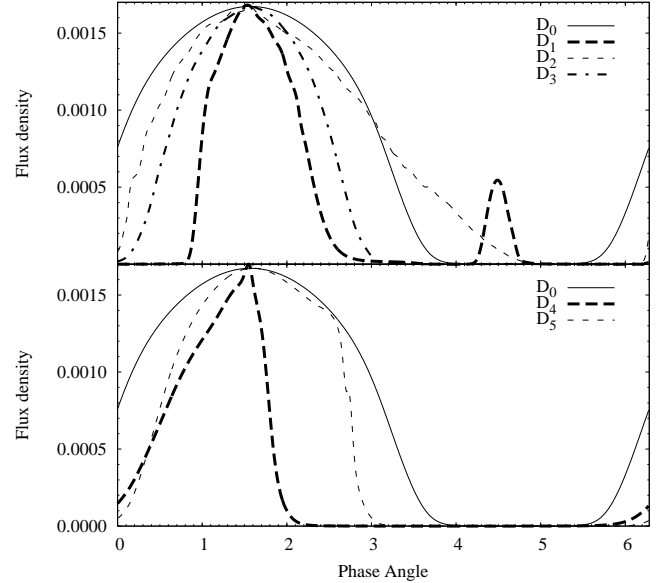


Figure 7. As for Fig. 3 but with an optical depth multiplier range of 4.0 to 14.0.

large $\Delta\tau$ in eq.(8), and to begin from a rather low value of τ_{min} , so that the range includes a substantial amount of unsaturated growth. However, another consideration is observability: a very large amplitude in the maser response is no good if the flare maximum is still too weak to see. A good compromise, perhaps, is to set τ_{max} in the moderately saturated regime, whilst τ_{min} is in the range that is essentially unsaturated. In Fig. 7 we show the light-curves resulting from the optimally oriented prolate cloud with $\tau_{min} = 4.0$ and $\Delta\tau = 10.0$. This set of curves maintains a maximum flux density that is only 0.47 times the maximum at the highly saturated depth multiplier of 29.0, whilst starting from a depth multiplier low enough to yield a variability index of 1.65×10^4 . Even the D_0 function in Fig. 7 has a broad range that appears indistinguishable from the baseline on this linear graph. However, saturation

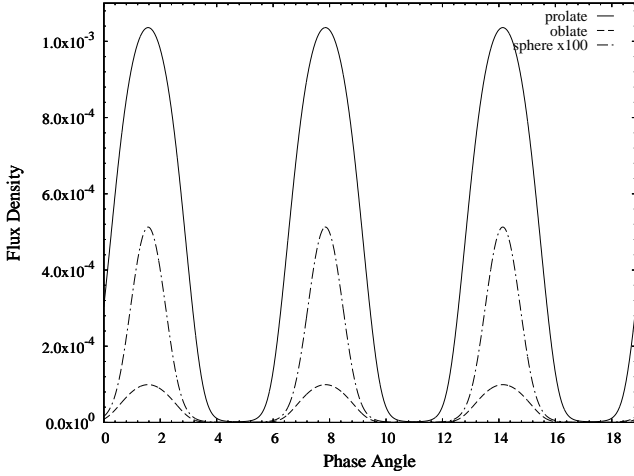


Figure 8. Maser light curves for the prolate (solid line), oblate (dashed line) and pseudo-spherical (chained line) clouds driven by function D_0 over three cycles with maser depth range 5-10. Note that the plotted light curve of the spherical cloud is multiplied by 100 to make it distinct from the x axis.

near maser maximum prevents the peak narrowing to a form with a much smaller duty cycle.

5.3 Effect of Cloud Shape

We compare here results for a pseudo-spherical cloud, and an oblate cloud with the same magnitude of distortion as the prolate cloud studied in Section 5.1 and most of the more general Section 5. To reduce complexity, only the default driving function D_0 is considered. We plot the maser response to this function for the three cloud shapes, over three periods, in Fig. 8. The range for the maser depth multiplier τ is 5-10, as in Fig. 4. The observer's position is 'optimum' for the prolate and oblate clouds. For an oblate cloud, this must lie close to the xy plane, and we have used $(\theta, \phi) = (\pi/2, \pi/2)$. We have used the same 'typical' position as in Section 5.1 for the pseudo-spherical object. We note from Paper 1 that variation of the viewing point for clouds of this type may alter the maser output by a factor of up to ~ 3 , but the maximum flux density of the spherical cloud in Fig. 8 is more than two orders of magnitude lower than that of the optimally viewed prolate cloud of the same volume. The respective variability indices for the prolate, oblate and pseudo-spherical clouds in Fig. 8 are 502, 2930 and 1760. The variability index of the prolate cloud is the smallest of the three because it has the highest minimum in Fig. 8, due to its geometry, whilst its maximum is significantly affected by saturation. The minima of all three curves merge with the x axis in Fig. 8 due to the linear flux density scale.

Over the partially saturated depth multiplier range of 10.0-15.0, as used in Fig. 3, the maximum flux density achieved with the oblate cloud was 3.0×10^{-4} , a factor of 5.99 smaller than in the prolate case. The pseudo-spherical object was weaker still, with a maximum flux density of 7.05×10^{-5} . Light curves for this depth multiplier range are not plotted, but their respective variability indices were 1.74, 3.03 and 13.52 for the prolate, oblate and pseudo-spherical clouds, implying that the light curves of the oblate and spherical clouds are somewhat less affected by saturation. The shape of the light curve for the oblate cloud is not significantly different from the prolate case, with the strong saturation flattening towards higher optical depth multipliers, as in Fig. 3.

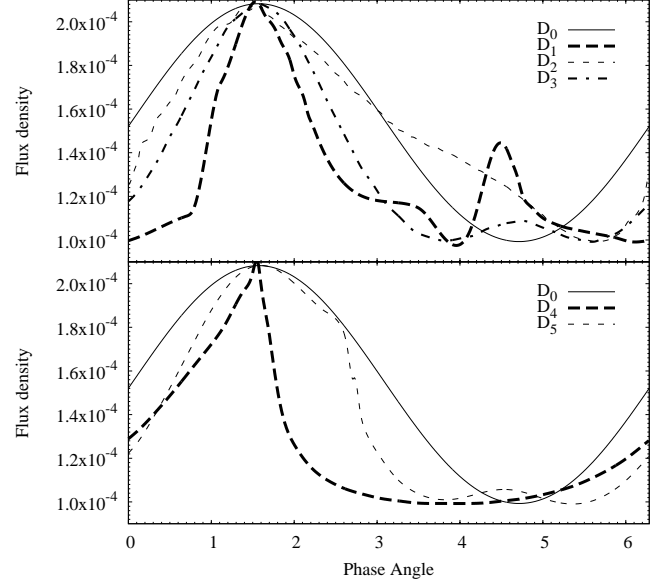


Figure 9. As Fig 3 but for a cloud with an unsaturated inversion profile that follows a $1/r^2$ function, where r is the radial distance from the cloud centre.

Even at the ultimate saturation level modelled, $\tau = 30$, the optimally viewed prolate cloud, with a flux density of 3.67×10^{-3} is still 4.83 times brighter than the optimally viewed oblate cloud, and 12.2 times brighter than the spherical cloud.

When shifted to the typical position, and here the same position is used for all types of cloud, we find that the maser flux density follows a qualitatively similar family of curves to those in Fig. 6. However, the maximum flux density order is now reversed with the spherical cloud at 5.22×10^{-6} being 19.84 times brighter than the oblate cloud and 22.93 times brighter than the prolate cloud. In terms of variability index the order is spherical, prolate, oblate with respective indices 1760, 502 (as in Fig. 6) and 341, indicating that the pseudo-spherical cloud is also the least affected by saturation from this viewpoint. However, the oblate cloud has the largest improvement in variability index by dropping the depth range to 5-10 from 10-15 from the optimum viewpoint.

5.4 Clouds with Internal Structure

The clouds introduced here have an unsaturated inversion that increases towards the centre of the cloud. As discussed in Section 2.4, this situation most likely corresponds to a case where the optical depth to the pumping radiation is fairly low, and a real increase in the number density of the maser molecule more than outweighs any decrease in the energy density of the pumping radiation towards the cloud centre. In Fig. 9, we show a situation comparable to that in Fig. 3 in terms of the minimum and maximum optical depth multipliers considered, and the optimally placed observer.

The effects of moving to a variable density cloud are not particularly profound, at least in terms of flux density. The curves in Fig. 9 strongly resemble those in Fig. 3, indicating a similar degree of saturation, but at a generally lower flux density. The variability index of the flare in Fig. 9 is 2.1. These results are consistent with the data shown in Fig. 2, where the spectra also show that the internally variable object also achieves a lower flux density for the same maser depth. If a different observable parameter is chosen, the brightest specific intensity of any ray, results from the inter-

nally variable object are more spectacular: this parameter reaches 19900 times the saturation intensity in the variable case, compared to 7000 in the internally uniform case. This parameter is only practically measurable in VLBI observation, and it is apparent from the images in Fig. 2 that a small number of very high intensity rays are not enough to compensate, in flux density, for many low intensity neighbours.

It is also interesting to shift the observer's viewpoint to the 'typical' position in the variable unsaturated inversion case. The result is a low-gain light-curve. The highest flux density achieved is only 7.00×10^{-7} with a variability index of 1.64. This index is lower than in the optimum case, and indicates a more saturated light curve. In the lower depth range of $\tau = 5 - 10$, the light-curve is almost twice as bright as that in Fig. 6, but unlike that case, it already shows significant signs of saturation. At this point, we end our discussion of sample light curves, and defer consideration of some variability parameters extracted from a much wider range of data to Section 7.

6 VARIABLE BACKGROUND RESULTS

Here we show results for driving functions D_0 and D_6 fitted to eq.(9). Function D_6 is chosen because it is particularly associated with variation of the background radiation. Parameters are now the minimum background level $i_{BG,min}$ and the range through which the background intensity varies, Δi_{BG} . We begin with results for the prolate cloud with uniform inversion, with the observer in the optimum viewing position. In Fig. 10 we adopt the largest value of Δi_{BG} covered by the computations, that is $\Delta i_{BG} = 10^4$. This implies that $i_{BG,min}$ is 10^{-9} of the saturation intensity, and the maximum background attained is 10^{-5} . Each panel of Fig. 10 shows light curves for a different value of the depth multiplier, which increases from 5.0 in the lowest panel to 10.0 in the top panel.

In the lowest panel of Fig. 10, the cloud is only weakly saturated, but the light curves here strongly resemble the original driving functions from Fig. 1. This is in contrast to the radiative pumping model, where the light curves would show strong near-exponential growth, as in, for example, Fig. 6. As the depth rises, we see a trend that is qualitatively different to anything seen in the work on radiative pumping. The trend is towards a constant saturation level (which rises somewhat with depth) with a narrowing drop-out to a significantly lower flux density near the lowest values of the driving function. The situation in the upper panel of Fig. 10 could perhaps be described as an 'anti-flare', where the light curve has a duty cycle tending to 1, and the high state of the curve is what an observer would mostly expect to see.

An expected trend with increasing saturation is a falling variability index, and this is indeed what is seen in moving from the bottom to the top panel in Fig. 10, where the respective variability indices are 8300, 421 and 1.66. If the depth multiplier is increased to 15.0, the maximum flux density rises to 2.12×10^{-3} and the variability index reduces to just 1.23. In fact, the duty cycle behaviour inverts from large ($\lesssim 1$) to very small (< 0.1) above a depth multiplier of ~ 12 . This regime is discussed in Section 7, but is not very interesting from the point of view of major flares because of the very small values of the variability index.

As the change in background that has been applied so far might be considered rather large, further light curves were computed with $i_{BG,min} = 10^{-8}$ and $\Delta i_{BG} = 250$. These additional light curves are displayed in Fig. 11. The results in Fig. 11 are in line with expectations, given the high duty cycle effect carried over

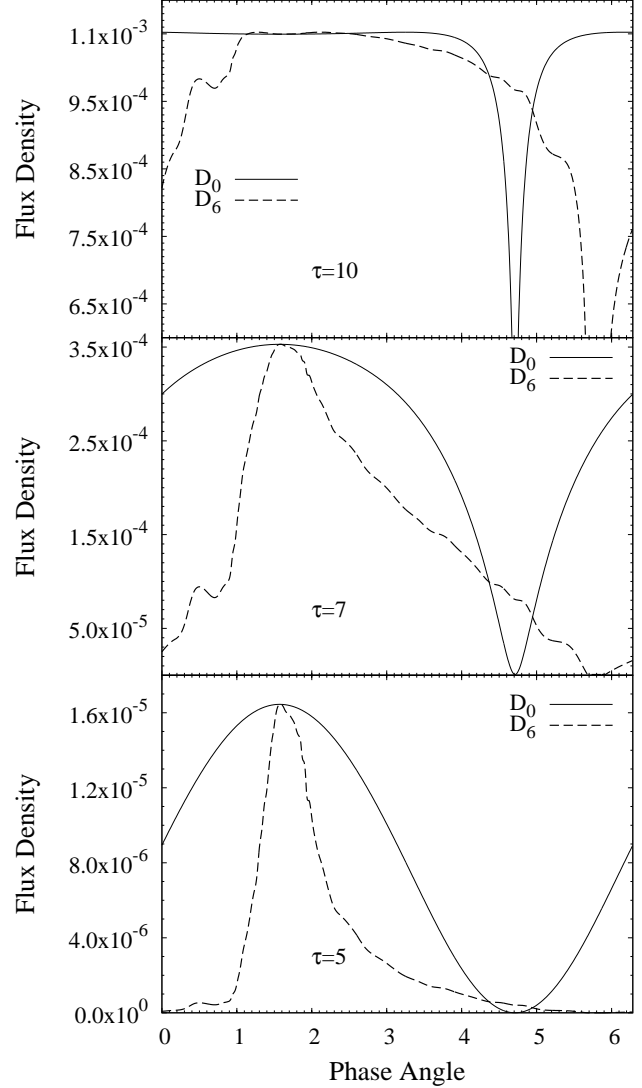


Figure 10. Maser light curves resulting from variation of the background radiation level that follows the form of the driving functions D_0 and D_6 . The minimum background level is 10^{-9} and the range is 10^4 . Panels represent calculations at different depth multipliers of, from bottom to top, $\tau = 5.0, 7.0$ and 10.0 .

from Fig. 10: saturation levels are lower, and the unsaturated behaviour, where the maser light curves resemble the driving functions, is maintained to higher values of τ .

Other variations do not change the qualitative behaviour shown in Fig. 10 and Fig. 11. Details follow the expectations from Sections 5.1-5.4. Viewpoints away from the cloud long axis lead to optically thinner behaviour and lower flux densities. Replacement of the prolate cloud with oblate and spherical shapes yield lower flux densities generally, and lower limiting flux densities at saturation. Use of clouds with internal variation in the unsaturated inversion shift the maser response at a given value of the optical depth multiplier towards somewhat thinner behaviour.

7 VIEWPOINT STATISTICS

The light curves discussed in Section 5 are just examples drawn from a wide range of possible parameter values far too extensive to

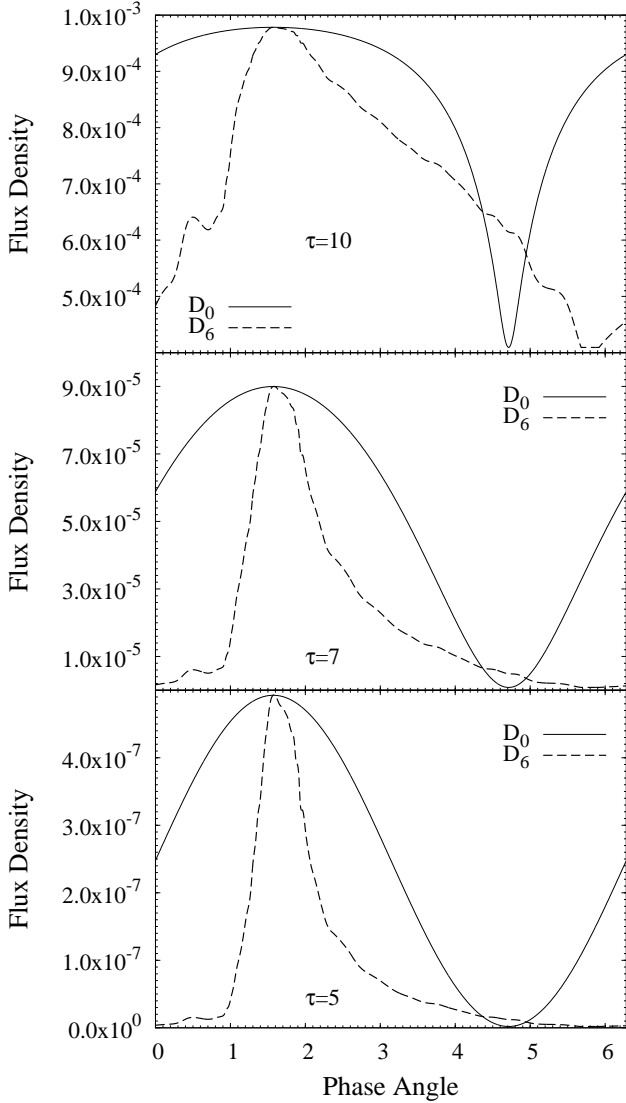


Figure 11. As for Fig. 10, but with a minimum background level of 10^{-8} and a range of 250.

plot out in a paper of this type. Therefore, we summarise a considerable quantity of data by extracting three important statistics from the light curves: the variability index, the duty cycle (as defined in Section 5), and the maximum flux density achieved. Each of these are plotted as a function of both $\Delta\tau$ and τ_{min} for two extreme example types: a prolate cloud with uniform unsaturated inversion, and an oblate cloud with the unsaturated inversion obeying a $1/r^2$ function. Here, both of these cloud styles are viewed from close to their respective optimum observer's position. The maximum flux density achieved is shown on a logarithmic scale via the colour palette in Fig. 12-13. In these same figures, black contours show the variability index and red contours, the duty cycle.

Results for the prolate cloud with uniform internal physical conditions are shown in Fig. 12. The first point to note is that saturating flux densities are achieved across most of the plotted plane, so the great majority of masers on it would be observable, given the cloud shape and privileged observer's position. The second point is that there is a minimum depth multiplier - approximately 7.5 - above which it is impossible to generate a large amplitude flare (variability index >10) via variation in the maser pumping. A third

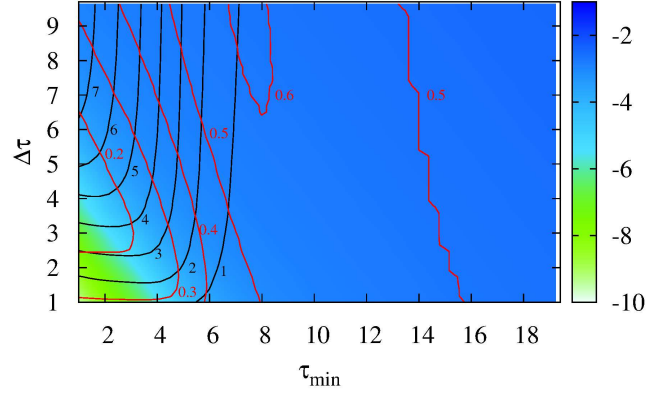


Figure 12. Three observable statistics as a function of minimum depth parameter and depth parameter change. These are: the maximum flux density achieved over the period, where the colour table represents the \log_{10} of the flux density, the variability index (black contours with levels indicating the \log_{10} of this quantity), and the duty cycle (red contours with values as marked). The background level is $i_{BG} = 10^{-6}$, and results are for driving function D_0 only, as applied to an internally uniform $\Gamma = 0.6$ prolate cloud.

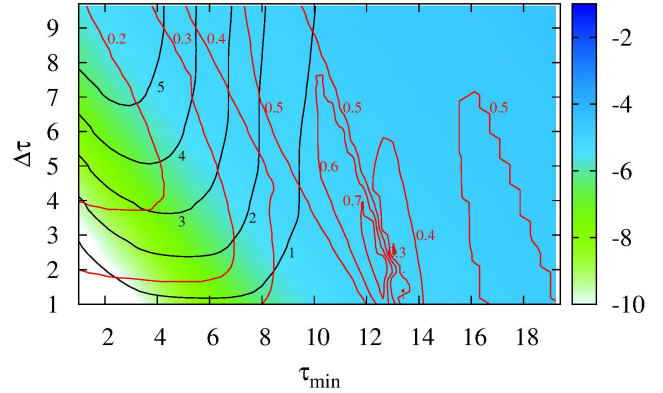


Figure 13. As for Fig. 12, but for the oblate cloud with internal structure. The observer's viewpoint is in the xy plane.

point is that variability index contours have an almost horizontal section that loops back to the $\Delta\tau$ axis, so there is also a minimum variation to the depth multiplier required to give a certain flare amplitude: a variability index of a million can be achieved with $\Delta\tau \geq 5$ for example. A fourth point arises with regard to the duty cycle: pumping variation is unlikely to produce values much above 0.5: large $\Delta\tau$ and $\tau_{min} \sim 8$ are required to achieve 0.6, whilst duty cycle values <0.3 are associated with unsaturated amplification.

As discussed above, the main effects of moving to an oblate cloud, even when viewed close to its optimum plane, and of changing to an internally structured object, are to reduce the maximum flux density of the maser and the variability index of flares. One more example is shown in Fig. 13: the counterpart of Fig. 12 for an oblate cloud with a $1/r^2$ function in its unsaturated inversion. The maximum variability index is now reduced to a number in the hundreds of thousands, and the model has thinner behaviour generally as expected. However, lower black contours representing variability indices of 10-100 survive to larger values of τ_{min} than in Fig. 12. There is also some interesting behaviour in the duty cycle, where there is a steep gradient at low $\Delta\tau$: the value of this param-

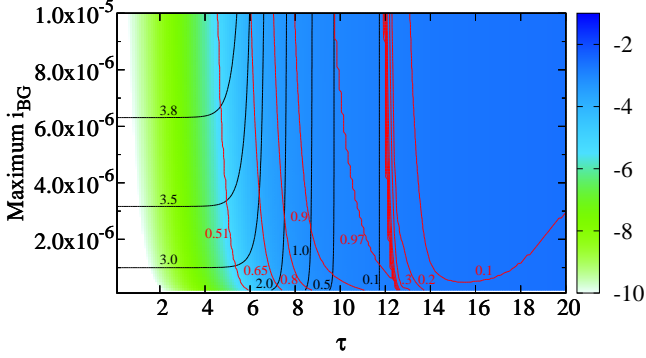


Figure 14. Statistics and cloud structure as for Fig. 12, but now plotted against optical depth multiplier, τ , and the maximum background intensity achieved by the driving function in each model. The minimum background intensity in all models used by this figure was 10^{-9} times the saturation intensity. The broad red region in this figure is a zone of closely-spaced contours, where the duty cycle switches rapidly from very high values to very low. This region is discussed in the text. The light curves plotted in Fig. 10 correspond to points in the present figure at the tops of vertical slices with $\tau = 5, 7$ and 10 .

eter falls from above 0.7 to ~ 0.3 over a small range of τ_{min} from approximately 12.0 to 13.0.

When the background intensity is varied with time, rather than the pumping radiation, a rather different pattern emerges from those in Fig. 12 and Fig. 13. Although results are somewhat dependent also on the minimum intensity of background radiation chosen, we show in Fig. 14 the same three statistics as in the previous two figures, now as a function of optical depth multiplier (x axis) and the maximum background intensity used in each model (y axis). The model cloud is the internally uniform prolate type, as used in Fig. 12. The y axis values are scaled to the saturation intensity, and the minimum background intensity used in all the models used to build Fig. 14 was 1.0×10^{-9} . The variability index of the driving functions is $10^{-7}/10^{-9} = 100$ at the bottom of Fig. 14 and 10000 at the top. In fact, it appears that the variability index of the maser response cannot exceed that of the driving function, unlike the variable pumping case, but it can be reduced by saturation.

Figure 14 can be conveniently divided into three regions from left to right along the τ axis. The unsaturated models in the left-most part, where $\tau < 4$, have a variability index that varies with the maximum background intensity, but is almost independent of τ , whilst the duty cycle is everywhere very close to 0.5. A particularly interesting region of Fig. 14 exists for intermediate depth multipliers, in the approximate range 4-14, where both the variability index and duty cycle become quite strong functions of the optical depth multiplier, but comparatively weak functions of the maximum background intensity. In this region, the variability index decreases monotonically through the value of $10^{0.1} \simeq 1.26$ at a depth multiplier of ~ 12 . The behaviour of the duty cycle in this depth range is first to increase to values close to 1.0 (the ‘anti-flare’ behaviour exemplified by the top panel of Fig. 10), and then to very rapidly fall as the narrow ‘hole’ in the light curve becomes a low amplitude, but still narrow, spike. On the high-depth side of this boundary, it is the lowest background intensity that gives rise to the highest maser flux density, contrary to the situation found at lower values of τ . Although low values of the duty cycle are found in this central portion, they are associated with such low levels of variability, that any flares of significant variability index (a factor of 1.26 or more) would be associated with values of the duty cycle above 0.5.

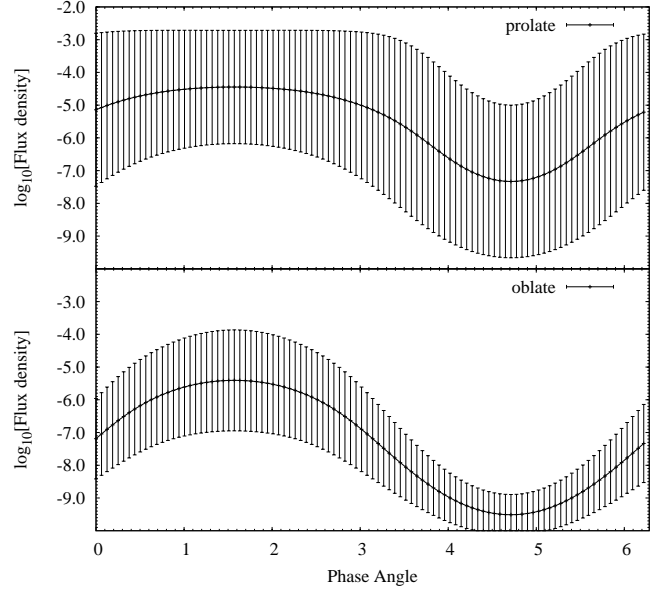


Figure 15. The base 10 logarithm of the mean light curve for $\tau_{min} = 5$ and $\Delta\tau = 5$ for a prolate cloud with uniform unsaturated inversion (upper panel) and an oblate cloud with $1/\tau^2$ unsaturated inversion (lower panel). Error bars are plotted in both panels, marking the sample standard deviation, and the mean in both cases is over 1000 random observer’s positions. Curves are responses to driving function D_0 only.

In the high saturation region of Fig. 14 the variability index is low, and continues to fall towards 1.0. The effect of the narrow spike in the light curve keeps the duty cycle low, but, as the 0.1 red contour suggests, at extreme saturation the duty cycle rises again, but no limiting value had been reached by a depth of $\tau = 30$.

The final plot in this Section, Fig. 15 shows the effect of varying the observer’s viewpoint in a more general sense than in Section 5.1. Formal solutions were obtained for 1000 randomly chosen observer’s viewpoints for the cases of a prolate cloud with uniform unsaturated inversions and an oblate cloud with the unsaturated inversions obeying a $1/\tau^2$ function. The cloud shapes and structures therefore follow those used in Fig. 12 and Fig. 13. The values of τ_{min} and $\Delta\tau$ used were both 5, so the range in depth is the same as in Fig. 4. The curves plotted in Fig. 15 show the maser flux density on a logarithmic scale to make the pattern of error bars clear; these show the sample standard deviation and represent the envelope of likely values of the flux density. Again, for reasons of clarity, only the response to the default driving function D_0 is shown.

The maser response in the upper panel of Fig. 15 is clearly strongly influenced by saturation, with the upper envelope limited to values of the flux density a little higher than 10^{-3} . The mean is less affected, but at the peak of the cycle it is ~ 100 times weaker than the saturation limit. The oblate cloud has a generally thinner envelope spanned by the error bars, and is less affected by saturation. The latter observation is expected from the behaviour discussed in Section 5.3 and Section 5.4. A typical cloud of this type will yield a flare of greater variability index than the prolate cloud in the upper panel of Fig. 15, but will have a peak flux density about an order of magnitude lower, a crucial consideration for detectability.

8 COMPUTING DETAILS

The non-linear Orthomin(K) algorithm (see Paper 2 and references therein) is still the core routine used in the present work to calculate nodal solutions. This algorithm has now been tested up to optical depth multipliers of 50.0: almost certainly considerably beyond the validity of the CVR approximation used in the present work. A single iteration job on the DiRAC dial machine at Leicester takes 10 s wall-time on the standard (dirac25x) queue. As in previous work in Papers 1 and 2, time taken for other computational tasks is negligible.

9 DISCUSSION

Saturation has a profound smoothing effect on maser variability driven by both the variable pumping and variable background mechanisms. This smoothing is stronger than in the case of rotation. For example, Fig. 11 of Paper 2 shows that both prolate and oblate clouds with $|\Gamma| = 0.6$ can yield flares with a variability index >30 at a depth multiplier of 13.0. In the present work, Fig. 12 and Fig. 13 indicate that the variability index is <10 at this depth. For the specific example of Fig. 3 that includes 13.0 in its depth range, the variability index is only 1.8. Even strongly peaked driving functions, such as D_1 give rise to maser light curves that are flatter near the peak when the depth is varied between 10.0 and 15.0. Their troughs are less affected.

Modest saturation acts to increase the duty cycle function in both the variable pumping and variable background mechanisms and, more generally, to remove the special identity of individual driving functions in parts of light curves that are at high flux density. Saturation cannot, however, extend the decay with respect to the rise time, or vice-versa. Extreme saturation, with variable pumping, produces response curves that have a shape that strongly resembles the driving functions: this is probably as expected, since a highly saturated maser is said to behave like a linear converter of inversion to photons, for example, Elitzur (1992). The variability index of the flare continues to reduce with depth multiplier, and the variability index for the 24.0-29.0 model (see Fig. 5) is only about 1.22, barely above the 1.21 for the driver. It is therefore difficult to get a large-amplitude flare from IR pumping in a saturated maser cloud. The best possibilities for easing the restrictions imposed by saturation are changing the internal distribution of the unsaturated inversion (or of the pumping rate) and changing the saturation intensity of the maser. The latter effect does not change the results presented in this work, which are scaled to this parameter, but would increase the achievable dimensioned flux densities, as discussed in Appendix A.

If the light curve of the IR pumping radiation is known at, or close to, the frequency of an important pumping transition, then comparison with the light curve of the maser offers a method of measuring the level of saturation in the maser cloud. Both the variability index and the duty cycle depend on the base level of maser depth and the range over which it is changed by the IR driving function. Therefore, these quantities can be read off a more detailed version of a plot like Fig. 12 by finding the best fit to the black and red contours.

Shifting the observer's position away from privileged viewpoints close to the long axes of clouds has a strong thinning effect. Whilst this allows for perhaps greater values of the variability index, and lower duty cycles, it also reduces the mean flux density considerably: a factor of 4500 in the 'typical position' example

from Fig. 6, but two orders of magnitude more generally from the averaged light curve for the prolate uniform cloud (upper panel of Fig. 15). These reductions suggest that the objects we see as bright flaring masers probably are those that are oriented rather favourably towards us, and another 'alien' observer in a different part of the Galaxy might see a different subset of objects. This suggestion is supported by the very poor performance of the pseudo-spherical cloud in the shape comparison in Fig. 8. Changing from a prolate to an oblate cloud has effects that are quite consistent with those found in Paper 2. The oblate cloud gives somewhat less amplification and saturation from a privileged viewpoint, but this is compensated for by a smaller standard deviation, so that the loss of flux density from a random viewpoint is less pronounced.

In terms of a combination of raw flux density and high variability index, the best maser flare candidates are obtained from prolate clouds viewed near the optimum orientation. A variability index of over 10^7 can be obtained (see Fig. 12) by starting from an object with extremely low saturation ($\tau_{min} < 1$) and applying a driving function with an amplitude of at least 7. Such an object would still achieve a peak flux density close to the saturating level, and so be detectable.

Use of clouds with an internal variation of the unsaturated inversion that behaves like $1/r^2$ has a strong thinning effect: for a given depth multiplier, the internally variable cloud gives a lower output, at least in terms of flux density. If instead the peak specific intensity found in an image is chosen as the parameter to view, it is typically larger in the internally variable cloud, at least from the privileged observer's viewpoint. However, as the images in Fig. 2 suggest, the very high brightness rays are of very limited number and area in the image of the internally variable cloud, and are not adequate to make up for a larger number of somewhat less bright rays when computing the flux density. The overall thinning effect is also supported by the histogram of nodes in various bands of saturation in Fig. 2. The cloud in Fig. 2 is oblate, and viewed in the xy plane. A more general conclusion about the flux density behaviour for an internally variable object of this type comes from the lower panel of Fig. 15. The typical level of the mean in this figure is an order of magnitude below the uniform prolate object, so internal variation of this type is unlikely to produce the most powerful flares. However, a form of internal variation that weights unsaturated inversions towards the cloud surface might produce larger flux densities for a given driving amplitude.

Variation of the background intensity is qualitatively different in at least two respects: firstly, the variability index is always reduced below that of the background variation itself, particularly at higher values of the depth multiplier. Observationally, maser variability must be accompanied by radio continuum variability of at least the same amplitude at the frequency of the maser transition. Secondly, the light curves that result from background variability have a characteristically higher duty cycle at moderate maser depths, where the variability index is $\gtrsim 1.26$. This effect is very apparent in Fig. 14, and in the upper two panels of Fig. 10 and the top panel of Fig. 11. The duty cycle parameter is likely a good discriminator between maser variability driven by background variation, where values in the range 0.6-0.9 are common, and pumping-driven variability, where values of the duty cycle >0.6 are rare. It is true that lower duty cycles can be obtained at both lower, and higher, values of the maser depth multiplier, but in the former case detectability is limited by lower, unsaturated, flux densities, whilst in the latter regime the variability index is too low to be relevant to strong flaring events.

If a particular maser flare event has been positively identi-

fied as resulting from background variability, then the duty cycle is potentially also a very good diagnostic of saturation and/or the applied Δi_{BG} , provided that it can be compared with the driving function, another need for high-cadence data at radio as well as IR wavelengths. For aperiodic and temporally isolated flares, however generated, a modified duty cycle parameter may still be defined. For example, if a flare is detected after a long quiescent period, the modified parameter could be defined as the fraction of the total time for which the light curve is above, say, the 5σ level of any minor variability during the quiescent phase.

As a test of the duty cycle as a discriminator between driving mechanisms, and the ability to derive flare parameters from our model, we attempt an analysis of the G107.298+5.63 periodic flare source, where both IR and maser light curves exist. From Fig. 3 of Stecklum et al. (2018), the maser has a duty cycle of about 5 days in 35, or $1/7 \approx 0.143$, whilst the driving light curve, our function D_1 has a duty cycle of 0.2, so the maser duty cycle is reduced by a factor of $0.143/0.2 = 0.72$ with respect to the IR driver. Since our Figures 12-14 are based on function D_0 , rather than D_1 , we suggest that the most reasonable comparison is to use the same reduction factor, placing G107.298+5.63 on the $0.5 \times 0.72 = 0.36$ duty cycle contour. The -7.4 km s^{-1} methanol maser spectral feature in G107.298+5.63 has a variability index of 120 (Szymczak et al. 2016), and it turns out that we can find positions of coincidence for this value and a duty cycle of 0.36 in both Fig. 12 and Fig. 13, but not in Fig. 14. We therefore reject the variable background mechanism for the flaring 6.7-GHz methanol masers in G107.298+5.63. For Fig. 12, the model parameters read off the axes are approximately ($\tau_{min} = 5, \Delta\tau = 3$); corresponding parameters in Fig. 13 are (7.5, 4.5). We proceed to check that the model flux densities at these positions is consistent with an observed value of approximately 50 Jy. The relevant model flux densities are $f_\nu = 4.5 \times 10^{-4}$ at (5, 3) in Fig. 12, and $f_\nu = 5.1 \times 10^{-6}$ at (7.5, 4.5) in Fig. 13. These numbers can be checked for consistency via eq.(A6) with a source distance of $d_{kpc} = 0.76$ and $Z = 0.79 \text{ Hz}$. For Fig. 12, a cloud size of $R_{AU} = 4.8$ is required; for Fig. 13 a larger size of 45 AU is needed. Both these sizes are consistent with the 30-80 AU region containing some clouds of both (methanol and H_2O) species (Szymczak et al. 2016). However, the fact that multiple clouds exist in a region of this size suggests that the smaller estimate of 4.8 AU from Fig. 12 is the more likely.

A similar analysis could possibly be attempted for S255-NIRS3, using the light curve from Uchiyama et al. (2019) as a driving function. We comment briefly here, but leave a quantitative analysis to a future publication. Data associated with the IR light curve show that the variability index (3400) of the methanol maser component at 6.42 km s^{-1} , the brightest, is much higher than that of the K_s band IR light curve (23). This would appear to rule out a variable background mechanism, but the variability index, and indeed the light curve, for the continuum at 6.7 GHz are unknown. We do note from Fig. 2 of Caratti o Garatti, Stecklum et al. (2017) that the flux density of the burst spectrum rises more quickly towards longer wavelengths than the pre-burst counterpart, leading to larger variability indices at longer wavelengths. However, it would be most unwise to extrapolate this trend very far. Purely from the point of view of the shapes of the maser response and driving light curves, assuming the radio continuum follows the IR pattern with sufficient amplitude, a variable background mechanism is favoured. We note that our function D_6 is a rough approximation to the light curve in Uchiyama et al. (2019), and that the shape of the maser response in Fig. 3 of Uchiyama et al. (2019), with its increased duty cycle with respect to the driver, resembles somewhat the dashed

(D_6) light curves in the middle panel of Fig. 10 and the top panel of Fig. 11.

Future work, in addition to a detailed analysis of S255-NIRS3, should include a fuller analysis of the effects of a pump-dependent saturation intensity, as discussed in Appendix A. The only parameter in eq.(5) that is scaled to the saturation intensity is i_{BG} . If this becomes a function of the mean intensity in the pumping radiation, the effect is to shift the chosen nodal solution from one of the family at the original i_{BG} to one from the family at lower (higher) i_{BG} as the pump mean intensity rises (falls). Overall, the effect is to couple pumping and background variability, though the effects are likely to be small, given the weakness of the maser response to background variation. Programmes are also underway to model flares generated by line-of-sight overlap of clouds and by shock compression. It is also hoped that more, and better, IR data for maser flare sources of all types will enable detailed analyses to be carried out, based on specific driving light curves, as we have attempted in a limited way for G107.298+5.63.

10 CONCLUSIONS

Maser flares of very high variability index ($>10^7$) can be generated by variation in the pumping radiation, provided that the maser cloud is initially very optically thin in the maser transition, and the change in maser depth over a cycle of the light curve includes a substantial portion of unsaturated growth. Detectability, or maximum flux density achieved, is optimised if the maser clouds are of prolate spheroidal shape, perhaps elongated towards an almost filamentary structure, and viewed close to the long axis of the cloud. Compared to rotation of irregular objects, variable pumping is a poor mechanism of generating flares from already saturated maser clouds.

Flares generated from variation in the background radiation at the maser frequency commonly have high duty cycles if detectable flux density and strong flaring variability are also requirements. The variability index of the flare is probably always smaller than that of the background variation. As with pumping variability, high initial saturation leads to a smaller variability index flare (or ‘anti-flare’, given the high duty cycle).

Clouds with an internal structure that makes unsaturated inversions larger towards the centre of the cloud result in lower flux densities than uniform clouds of the same depth multiplier. However, the structured clouds typically have a higher peak specific intensity (observationally, the brightest pixel in a VLBI image). Clouds of this type would therefore have narrower beam angles, and yield smaller spot sizes in VLBI images than internally uniform clouds of the same shape.

Further work should include full analysis of the case where the saturation intensity is itself a function of the pumping radiation, additional weighting functions for internal structure and full molecular energy level schemes to replace the current phenomenological pumping model.

ACKNOWLEDGMENTS

MDG and SE acknowledge funding from the UK Science and Technology Facilities Council (STFC) as part of the consolidated grant ST/P000649/1 to the Jodrell Bank Centre for Astrophysics at the University of Manchester. MDG acknowledges financial support from the National Astronomical Research Institute of Thailand

(NARIT) whilst on sabbatical at their HQ in Chiang Mai, Thailand. This work was performed, in part, using the DiRAC Data Intensive service at Leicester, operated by the University of Leicester IT Services, which forms part of the STFC DiRAC HPC Facility (www.dirac.ac.uk). The equipment was funded by BEIS capital funding via STFC capital grants ST/K000373/1 and ST/R002363/1 and STFC DiRAC Operations grant ST/R001014/1. DiRAC is part of the National e-Infrastructure. Data used in this work was generated under DiRAC award dp124.

REFERENCES

- Araya E. D., Hofner P., Goss W. M., Kurtz S., Richards A. M. S., Linz H., Olmi L., Sewilo M., 2010, *ApJ*, 717, L133
- Bhardwaj A., Kanbur S. M., Marconi M., Rejkuba M., Singh H. P., Ngeow C.-C., 2017, *MNRAS*, 466, 2805
- Bisyarina A. P., Sobolev A. M., Tatarnikov A. M., Shenavrin V. I., Aberfelds A., Shmeld I., Volvach A. E., 2018, in *Modern Star Astronomy. Vol. 1* Vol. 1, *Infrared Photometric Monitoring of Young Stellar Objects in Vicinity of Flaring Maser Sources*. pp 81–84
- Brand J., Engels D., Winnberg A., 2018, in Tarchi A., Reid M. J., Castangia P., eds, *Astrophysical Masers: Unlocking the Mysteries of the Universe* Vol. 336 of *IAU Symposium, Variability of water masers in evolved stars on timescales of decades*. pp 393–394
- Burns R. A., Orosz G., Bayandina O., Surcis G., Olech M., MacLeod G., Volvach A., Rudnitskii G., Hirota T., Blanchard e. a., 2020, *MNRAS*, 491, 4069
- Caratti o Garatti A., Cesaroni R., Moscadelli L., Stecklum B., Sanna A., Garcia Lopez R., Ray T., Eisloffel J., Oudmaijer R., de Wit W. J., 2017, *Mem. Soc. Astron. Italiana*, 88, 773
- Caratti o Garatti A., Stecklum B., Garcia Lopez R., Eisloffel J., Ray T. P., Sanna A., Cesaroni R., Walmsley C. M., Oudmaijer R. D., de Wit W. J., 2017, *Nature Physics*, 13, 276
- Chen Y., Cai D., 2001, *App. Maths. & Computation*, 124, 351
- Cragg D. M., Mikhtiev M. A., Bettens R. P. A., Godfrey P. D., Brown R. D., 1993, *MNRAS*, 264, 769
- Cragg D. M., Sobolev A. M., Godfrey P. D., 2005, *MNRAS*, 360, 533
- de Jong T., 1973, *A&A*, 26, 297
- Elitzur M., 1992, *Astronomical masers*. Kluwer, Dordrecht
- Endres C. P., Schlemmer S., Schilke P., Stutzki J., Miller H. S., 2016, *Journal of Molecular Spectroscopy*, 327, 95
- Etoka S., Gérard E., Richards A. M. S., Engels D., Brand J., Le Bertre T., 2017, *MNRAS*, 468, 1703
- Etoka S., Le Squeren A. M., 1997, *A&A*, 321, 877
- Field D., Gray M. D., de St. Paer P., 1994, *A&A*, 282, 213
- Frisch H., 1988, in *Saas-Fee Advanced Course 18: Radiation in Moving Gaseous Media Radiative Transfer with Frequency Redistribution - Asymptotic methods scaling laws and approximate solutions*. p. 339
- Fujisawa K., Takase G., Kimura S., Aoki N., Nagadomi Y., Shimomura T., Sugiyama K., Motogi K., Niinuma K., Hirota T., 2014, *PASJ*, 66, 78
- Goedhart S., Gaylard M. J., van der Walt D. J., 2004, *MNRAS*, 355, 553
- Goedhart S., Minier V., Gaylard M. J., van der Walt D. J., 2005, *MNRAS*, 356, 839
- Goedhart S., van Rooyen R., van der Walt D. J., Maswanganye J. P., Sanna A., MacLeod G. C., van den Heever S. P., 2019, *MNRAS*, 485, 4676
- Gray M. D., 2007, *MNRAS*, 375, 477
- Gray M. D., 2012, *Maser Sources in Astrophysics*. Cambridge University Press, Cambridge, UK
- Gray M. D., 2018, in *14th European VLBI Network Symposium & Users Meeting (EVN 2018) 3D Models of Maser Flares*. p. 73
- Gray M. D., Baggott J., Westlake J., Etoka S., 2019, *MNRAS*, 486, 4216 (Paper 2)
- Gray M. D., Baudry A., Richards A. M. S., Humphreys E. M. L., Sobolev A. M., Yates J. A., 2016, *MNRAS*, 456, 374
- Gray M. D., Mason L., Etoka S., 2018, *MNRAS*, 477, 2628 (Paper 1)
- Hirota T., Ando K., Bushimata T., Choi Y. K., Honma M., Imai H., Iwadate K., Jike T., Kamenno S., Kameya e. a., 2008, *PASJ*, 60, 961
- Hunter T., Bartkiewicz A., Briskeen W., Brogan C. L., Burns R., Chibueze J. O., Cyganowski C. J., Hirota T., MacLeod G., Sanna A., 2019, in *Bull. Am. Astron. Soc. Vol. 51, Understanding Accretion Outbursts in Massive Protostars through Maser Imaging*. p. 13
- Hunter T. R., Brogan C. L., MacLeod G., Cyganowski C. J., Chandler C. J., Chibueze J. O., Friesen R., Indebetouw R., Thesner C., Young K. H., 2017, *ApJ*, 837, L29
- Inayoshi K., Sugiyama K., Hosokawa T., Motogi K., Tanaka K. E. I., 2013, *ApJ*, 769, L20
- Kurayama T., Nakagawa A., Sawada-Satoh S., Sato K., Honma M., Sunada K., Hirota T., Imai H., 2011, *PASJ*, 63, 513
- MacLeod G. C., Smits D. P., Goedhart S., Hunter T. R., Brogan C. L., Chibueze J. O., van den Heever S. P., Thesner C. J., Banda P. J., Paulsen J. D., 2018, *MNRAS*, 478, 1077
- Moscadelli L., Sanna A., Goddi C., Walmsley M. C., Cesaroni R., Caratti o Garatti A., Stecklum B., Menten K. M., Kraus A., 2017, *A&A*, 600, L8
- Nugent C. R., Mainzer A., Masiero J., Bauer J., Cutri R. M., Grav T., Kramer E., Sonnett S., Stevenson R., Wright E. L., 2015, *ApJ*, 814, 117
- Parfenov S. Y., Sobolev A. M., 2014, *MNRAS*, 444, 620
- Press W. H., Teukolsky S. A., Vetterling W. T., Flannery B. P., 1992, *Numerical recipes in FORTRAN. The art of scientific computing*
- Rabli D., Flower D. R., 2010, *MNRAS*, 406, 95
- Rajabi F., Houde M., 2017, *Science Advances*, 3, e1601858
- Sanna A., Menten K. M., Carrasco-González C., Reid M. J., Ellingsen S. P., Brunthaler A., Moscadelli L., Cesaroni R., Krishnan V., 2015, *ApJ*, 804, L2
- Schöier F. L., van der Tak F. F. S., van Dishoeck E. F., Black J. H., 2005, *A&A*, 432, 369
- Shakhvorostova N. N., Vol'vach L. N., Vol'vach A. E., Dmitrova A. I., Bayandina O. S., Val'ts I. E., Alakoz A. V., Ashimbaeva N. T., Rudnitskii G. M., 2018, *Astronomy Reports*, 62, 584
- Shimoikura T., Kobayashi H., Omodaka T., Diamond P. J., Matveyenko L. I., Fujisawa K., 2005, *ApJ*, 634, 459
- Singh N. K., Deshpande A. A., 2012, in Booth R. S., Vlemmings W. H. T., Humphreys E. M. L., eds, *Cosmic Masers - from OH to H0* Vol. 287 of *IAU Symposium, Binary systems: implications for outflows & periodicities relevant to masers*. pp 93–97
- Sobolev A. M., Bisyarina A. P., Gorda S. Y., Tatarnikov A. M., 2019, *Research in Astronomy and Astrophysics*, 19, 038
- Sobolev A. M., Cragg D. M., Godfrey P. D., 1997, *A&A*, 324, 211
- Sobolev A. M., Gray M. D., 2012, in Booth R. S., Vlemmings W. H. T., Humphreys E. M. L., eds, *Cosmic Masers - from OH to H0*

Vol. 287 of IAU Symposium, Modelling of Cosmic Molecular Masers: Introduction to a Computation Cookbook. pp 13–22

Stecklum B., Caratti o Garatti A., Hodapp K., Linz H., Moscadelli L., Sanna A., 2018, in Tarchi A., Reid M. J., Castangia P., eds, Astrophysical Masers: Unlocking the Mysteries of the Universe Vol. 336 of IAU Symposium, Infrared variability, maser activity, and accretion of massive young stellar objects. pp 37–40

Stecklum B., Caratti o Garatti A., Klose S., Wiseman P., 2017, The Astronomer’s Telegram, 10842, 1

Strel’nitskii V. S., 1981, Soviet Astronomy, 25, 373

Strel’nitskii V. S., 1982, Soviet Astronomy Letters, 8, 86

Sugiyama K., Fujisawa K., Doi A., Honma M., Kobayashi H., Bushimata T., Mochizuki N., Murata Y., 2008, PASJ, 60, 23

Sugiyama K., Saito Y., Akitaya H., Yonekura Y., Momose M., 2017, The Astronomer’s Telegram, 10757, 1

Szymczak M., Olech M., Wolak P., Bartkiewicz A., Gawroński M., 2016, MNRAS, 459, L56

Szymczak M., Olech M., Wolak P., Gérard E., Bartkiewicz A., 2018, A&A, 617, A80

Szymczak M., Wolak P., Bartkiewicz A., 2015, MNRAS, 448, 2284

Torstensson K. J. E., van Langevelde H. J., Vlemmings W. H. T., Bourke S., 2011, A&A, 526, A38

Uchiyama M., Yamashita T., Sugiyama K., Nakaoka T., Kawabata M., Itoh R., Yamanaka M., Akitaya H., Kawabata K., Yonekura Y., Saito Y., Motogi K., Fujisawa K., 2019, PASJ, p. 129

Urquhart J. S., Moore T. J. T., Menten K. M., König C., Wyrowski F., Thompson M. A., Csengeri T., Leurini S., Eden D. J., 2015, MNRAS, 446, 3461

Uscanga L., Cantó J., Gómez J. F., Anglada G., Torrelles J. M., Patel N. A., Raga A. C., Curiel S., 2010, ApJ, 715, 132

van der Walt D. J., 2011, AJ, 141, 152

van der Walt D. J., Goedhart S., Gaylard M. J., 2009, MNRAS, 398, 961

van der Walt D. J., Maswanganye J. P., Etoke S., Goedhart S., van den Heever S. P., 2016, A&A, 588, A47

Vol’vach L. N., Vol’vach A. E., Larionov M. G., MacLeod G. C., van den Heever S. P., Wolak P., Olech M., Ipatov A. V., Ivanov D. V., Mikhailov A. G., 2019, Astronomy Reports, 63, 49

APPENDIX A: FLUX DENSITY UNITS

Formal solutions in the present model produce specific intensities in a number of rays that are scaled to the saturation intensity, I_{sat} , of the maser. In the IR pumping models, the background level is $i_{BG} = I_{BG}/I_{sat} = 10^{-6}$. A flux density is computed via a standard definition at a distance sufficient to make the rays almost parallel: by default, this distance is 1000 times the cloud scale (see below). Rays originate on a disc, slightly more remote from the observer than the cloud, that is designed to be larger than the cloud in any orientation. The slightly reduced version of this disc that passes through the cloud centre, has a radius R that we will call the cloud scale. The flux density is then

$$f_\nu = \sum_{j=1}^J i_j \cos \theta_j \delta \Omega_j, \quad (\text{A1})$$

where a particular ray has specific intensity i_j in saturation units, originates at an angle θ_j off-axis, as seen by the observer, and has a solid angle weighting of $\delta \Omega_j$, which is almost the same for all rays (see Paper 1).

When the cloud optical depth multiplier is zero, the cloud is transparent, and $i_j = i_{BG}$ for all rays. The background flux density, assuming negligible emission beyond the cloud scale is therefore,

$$f_{BG} = \pi i_{BG} (1/1000)^2, \quad (\text{A2})$$

For the standard $i_{BG} = 10^{-6}$ used in the IR pumping part of the paper, eq.(A2) reduces to $f_{BG} = \pi \times 10^{-12}$. A moderately saturating value of the flux density is then of order 10^{-6} – 10^{-5} , whilst values of $>10^{-3}$ indicate rather strong saturation.

A useful method of placing this scaled formula into something more familiar to observers is to place the distances in AU, and shift the observer to a standard distance of 1 kpc. For distances much larger than $R = 1$ AU, the flux density is proportional to $1/d^2$, and

$$f_{kpc} = f_\nu (R_{AU}/206265 d_{kpc})^2. \quad (\text{A3})$$

The remaining issue is that f_ν is scaled to the saturation intensity of the maser transition. This obviously depends on the particular transition studied. As a common example, we use the 6.7 GHz maser transition of methanol. The saturation intensity for a general maser is taken from Gray (2012) as

$$I_{sat} = (Z + A_{ij} + C_{ij} + C_{ji}) / (B_{ij} + B_{ji}), \quad (\text{A4})$$

where A_{ij} , B_{ij} are respectively the Einstein A and B coefficients for transfer across the maser transition, upper level i and lower level, j . The C coefficients are first-order collisional rate coefficients in the same transition, whilst Z is the all process rate coefficient for transfer from level i to all other levels excluding j and acts, for current purposes, like extra spontaneous emission. A data file from the Leiden Atomic and Molecular Database (Schöier et al. 2005), containing data from the CDMS (Endres et al. 2016), shows that $A_{ij} = 1.593 \times 10^{-9}$ Hz is negligible compared to other terms on the right-hand side of eq.(A4). This, and relations between the Einstein coefficients enable us to reduce the saturation intensity to

$$I_{sat} = \frac{2h\nu^3}{c^2(1 + g_i/g_j)} \left[\frac{Z + C_{ij} + C_{ji}}{A_{ij}} \right], \quad (\text{A5})$$

where ν is the maser frequency of 6.66852 GHz and $g_i/g_j = 11/13$ is the ratio of the statistical weights of the levels (Leiden data file). Second-order rate coefficients for the maser transition itself are also dwarfed by the collisional terms to other levels that form part of Z , and so can also be ignored at any density of collision partner. The result is that eq.(A3) can be reduced to the numerical version,

$$F_{kpc} \simeq 3500 Z (R_{AU}/d_{kpc})^2 f_\nu \text{ Jy}. \quad (\text{A6})$$

The remaining difficulty is the value of Z . Downward radiative transitions from the upper maser level make this at least 1.5×10^{-4} Hz. Upward radiative rates are harder to gauge because they involve a radiation mean intensity. A typical grey-body dust formula without attenuation or geometrical dilution yields a rate, within the data from the Leiden file, that is unlikely to exceed 10^{-3} Hz at any temperature (<250 K) used in the methanol models by Cragg et al. (2005). Again using data within the Leiden file, downward second-order rate coefficients (Rabli & Flower 2010) from the upper maser level sum to $3.21 \times 10^{-10} \text{ cm}^3 \text{ s}^{-1}$. Upward contributions are harder to calculate, but similar, suggesting that an overall approximation to Z is $\sim 6.5 \times 10^{-10} n_{H_2}$ Hz for an H_2 number density in cm^{-3} . From graphs in Cragg et al. (2005), 0.0065 Hz might be typical and 0.065 Hz rather high without quenching the maser.

Values of Z estimated above would yield a constant saturation intensity for a cloud with constant number density of H_2 and constant temperature. Adding collisional transfer to levels above the Leiden set is unlikely to make much difference owing to increasingly adverse Boltzmann factors. However, radiative transfer to levels in excited torsional states of methanol are also not included in the Leiden set, and are vital to pumping the 6.7-GHz maser. Einstein A-values for those transitions that couple the first and second torsionally excited states to the upper maser level can be found in Cragg et al. (1993). There are six such transition with A-values >0.01 Hz, the strongest being 0.297 Hz. This is not the whole story, as these transitions are upward with respect to the upper maser level, with a rate $B\bar{J}$ that depends on a radiation field. If the radiation comes from dust, the rate due to these lines will be approximately the sum of terms like,

$$B\bar{J} = A(e^{h\nu/(kT_d)} - 1)^{-1}(\lambda/\lambda_0)^{-p}, \quad (\text{A7})$$

where T_d is the dust temperature, A is the A-value and the wavelength ratio is a typical dust weighting term with $\lambda_0 \sim 80 \mu\text{m}$ and $p = 2$. The whole of eq.(A7) might also be multiplied by geometrical dilution and/or attenuation factors. A quick calculation using the six transitions introduced above for $T_d = 250\text{K}$ yields a value significantly faster than the collisional rate discussed above, that is $\sum B\bar{J} \simeq Z = 0.79$ Hz. With this value, eq.(A6) yields a dimensioned flux density for a 10 AU cloud at 1 kpc with $f_\nu = 10^{-3}$ of 280 Jy. However, through its dependence on \bar{J} , the saturation intensity itself now depends on the pump rate, allowing the dimensioned flux density to increase by a factor of typically a few over the rising part of the flare.